

9-2013

Surface ocean pCO₂ seasonality and sea-air CO₂ flux estimates for the North American east coast

SR Signorini

A Mannino

RG Najjar

Marjorie A.M. Friedrichs
Virginia Institute of Marine Science

et al

Follow this and additional works at: <https://scholarworks.wm.edu/vimsarticles>



Part of the [Oceanography Commons](#)

Recommended Citation

Signorini, SR; Mannino, A; Najjar, RG; Friedrichs, Marjorie A.M.; and et al, Surface ocean pCO₂ seasonality and sea-air CO₂ flux estimates for the North American east coast (2013). *Journal of Geophysical Research: Oceans*, 118(10), 5439-5360.
DOI: 10.1002/jgrc.20369

This Article is brought to you for free and open access by the Virginia Institute of Marine Science at W&M ScholarWorks. It has been accepted for inclusion in VIMS Articles by an authorized administrator of W&M ScholarWorks. For more information, please contact scholarworks@wm.edu.

Surface ocean $p\text{CO}_2$ seasonality and sea-air CO_2 flux estimates for the North American east coast

Sergio R. Signorini,¹ Antonio Mannino,² Raymond G. Najjar Jr.,³ Marjorie A. M. Friedrichs,⁴ Wei-Jun Cai,⁵ Joe Salisbury,⁶ Zhaohui Aleck Wang,⁷ Helmuth Thomas,⁸ and Elizabeth Shadwick⁹

Received 9 November 2012; revised 19 August 2013; accepted 20 August 2013; published 16 October 2013.

[1] Underway and in situ observations of surface ocean $p\text{CO}_2$, combined with satellite data, were used to develop $p\text{CO}_2$ regional algorithms to analyze the seasonal and interannual variability of surface ocean $p\text{CO}_2$ and sea-air CO_2 flux for five physically and biologically distinct regions of the eastern North American continental shelf: the South Atlantic Bight (SAB), the Mid-Atlantic Bight (MAB), the Gulf of Maine (GoM), Nantucket Shoals and Georges Bank (NS+GB), and the Scotian Shelf (SS). Temperature and dissolved inorganic carbon variability are the most influential factors driving the seasonality of $p\text{CO}_2$. Estimates of the sea-air CO_2 flux were derived from the available $p\text{CO}_2$ data, as well as from the $p\text{CO}_2$ reconstructed by the algorithm. Two different gas exchange parameterizations were used. The SS, GB+NS, MAB, and SAB regions are net sinks of atmospheric CO_2 while the GoM is a weak source. The estimates vary depending on the use of surface ocean $p\text{CO}_2$ from the data or algorithm, as well as with the use of the two different gas exchange parameterizations. Most of the regional estimates are in general agreement with previous studies when the range of uncertainty and interannual variability are taken into account. According to the algorithm, the average annual uptake of atmospheric CO_2 by eastern North American continental shelf waters is found to be between -3.4 and -5.4 Tg C yr⁻¹ (areal average of -0.7 to -1.0 mol CO_2 m⁻² yr⁻¹) over the period 2003–2010.

Citation: Signorini, S. R., A. Mannino, R. G. Najjar, Jr., M. A. M. Friedrichs, W.-J. Cai, J. Salisbury, Z. Aleck Wang, H. Thomas, and E. Shadwick (2013), Surface ocean $p\text{CO}_2$ seasonality and sea-air CO_2 flux estimates for the North American east coast, *J. Geophys. Res. Oceans*, 118, 5439–5460, doi:10.1002/jgrc.20369.

1. Introduction

[2] Coastal oceans, despite covering a small fraction of the earth's surface, are important in the global carbon cycle

because rates of carbon fixation, remineralization, and burial are much higher than the global average. A crucial difference between the coastal ocean and the open ocean is the proximity of sediments to the sea surface, providing a close coupling in space and time of the pelagic and benthic environments. Thus, the shallow water column in coastal regions constitutes a close link between surface sediments and the atmosphere allowing relatively direct interactions between both the sedimentary and atmospheric compartments [Borges *et al.*, 2005; Thomas and Borges, 2012; Thomas *et al.*, 2009; Thomas, 2004]. An additional characteristic of the coastal seas and continental shelves is the high temporal and spatial variability of CO_2 fluxes [Borges *et al.*, 2005, 2008; Cai *et al.*, 2006; Frankignoulle and Borges, 2001; Shadwick *et al.*, 2010, 2011]. The driving factors often vary within the system at seasonal time scales, and the deduction of general patterns remains difficult, typically requiring detailed case studies.

[3] The work of Borges [2005] was the first to compile a global coastal shelf sea-air CO_2 flux based on limited observed systems and using an upscaling scheme. Borges [2005] showed that the inclusion of the coastal ocean increases the estimates of CO_2 uptake by the global ocean by 57% for high latitude areas, and by 15% for temperate latitude areas, while at subtropical and tropical latitudes the contribution from the coastal ocean increases the CO_2

¹Science Applications International Corporation, Washington, D.C., USA.

²NASA Goddard Space Flight Center, Ocean Ecology Laboratory, Greenbelt, Maryland, USA.

³Department of Meteorology, The Pennsylvania State University, University Park, Pennsylvania, USA.

⁴Virginia Institute of Marine Science, College of William & Mary, Gloucester Point, Virginia, USA.

⁵School of Marine Science and Policy, University of Delaware, Newark, Delaware, USA.

⁶Institute for the Study of Earth, Oceans and Space, of New Hampshire, Durham, New Hampshire, USA.

⁷Department of Marine Chemistry & Geochemistry, Woods Hole Oceanographic Institute, Woods Hole, Massachusetts, USA.

⁸Department of Oceanography, University, Halifax, Scotia, Canada.

⁹Antarctic Climate and Ecosystems Cooperative Research Centre, University of Tasmania, Hobart, Tasmania, Australia.

Corresponding author: S. R. Signorini, NASA Goddard Space Flight Center, Code 616.2, Bldg 28/Rm W168, 8800 Greenbelt Rd., Greenbelt, MD 20771, USA. (sergio.signorini@nasa.gov or srsigno45@gmail.com)

emission to the atmosphere from the global ocean by 13%. *Cai et al.* [2006] conducted a study of sea-air carbon exchange in ocean margins by grouping the numerous heterogeneous shelves into seven distinct provinces. Their results showed that the continental shelves are a sink of atmospheric CO₂ at mid-high latitudes ($-0.33 \text{ Pg C yr}^{-1}$) and a source of CO₂ at low latitudes ($0.11 \text{ Pg C yr}^{-1}$), with a net uptake of $-0.22 \text{ Pg C yr}^{-1}$. *Laruelle et al.* [2010] evaluated the exchange of CO₂ between the atmosphere and the global coastal ocean from a compilation of sea-air CO₂ fluxes scaled using a spatially explicit global typology of continental shelves. Their computed sink of atmospheric CO₂ over the continental shelf areas ($-0.21 \pm 0.36 \text{ Pg C yr}^{-1}$) is at the low end of the range of previous estimates (-0.22 to $-1.00 \text{ Pg C yr}^{-1}$). *Laruelle et al.* [2010] also concluded that the sea-air CO₂ flux per surface area over continental shelves, $-0.7 \pm 1.2 \text{ mol CO}_2 \text{ m}^{-2} \text{ yr}^{-1}$, is twice the value of the open ocean based on the most recent CO₂ climatology at the time. More recently [*Cai*, 2011] showed that the continental shelves are sinks of atmospheric CO₂ ($\sim 0.25 \text{ Pg C yr}^{-1}$, but still with large uncertainty), accounting for $\sim 17\%$ of open ocean CO₂ uptake ($-1.5 \text{ Pg C yr}^{-1}$, *Takahashi et al.* [2009]). The largest uncertainty of these scaling approaches stems from the availability of CO₂ data to describe the spatial variability, as well as to capture the relevant scales of temporal variability.

[4] Given that relatively large amounts of carbon are exchanged via the sea-air interface in coastal seas and continental shelves, the knowledge of the seasonal and interannual variability of the sea-air CO₂ flux in coastal oceans is a very important component of the carbon budget, which requires comprehensive regional studies. In general, the coastal ocean is characterized by a high variability in carbon cycling, which presents significant challenges in determining spatial and temporal integrals of relevant quantities, such as the sea-air CO₂ flux. Therefore, innovative methods are needed for scaling up relatively sparse field measurements, in this case surface ocean *p*CO₂, into the required temporal and spatial resolutions to effectively derive regional sea-air CO₂ flux estimates. One method for obtaining such regionally integrated fluxes is through the use of biogeochemical circulation models, which can be evaluated using the sparse field measurements, and then used to compute the mean and variability associated with these regional fluxes [*Hofmann et al.*, 2011]. Satellite data, because of their high temporal and spatial resolution, provide another very promising asset to accomplish this goal. For example, *Lohrenz and Cai* [2006] conducted a satellite ocean color assessment of sea-air fluxes of CO₂ in the northern Gulf of Mexico. They used principal component analysis and multiple regression to relate the surface ocean *p*CO₂ to SST, salinity, and chlorophyll and used retrieval of corresponding MODIS-Aqua products to assess the regional distributions of *p*CO₂.

[5] In this paper, we use multiple regression analysis to relate surface ocean *p*CO₂ to environmental variables (SST, surface salinity, and chlorophyll) and use the resulting equations with inputs from corresponding satellite products to provide an assessment of the spatial and temporal variability of the surface ocean *p*CO₂ and sea-air CO₂ flux for the North American east coast. A brief description of the biological/physical setting of the study region is provided in section 2. The processing of in situ and satellite

data sets and the development of regionally specific empirical *p*CO₂ algorithms are described in section 3. The algorithm evaluation and the estimates of sea-air flux from the available *p*CO₂ binned data and algorithm are provided in section 4, as well as a sensitivity analysis of parameters that influence the surface ocean *p*CO₂ seasonal and interannual variability. Finally, we provide a summary and discussion of suggested future work in section 5.

2. Physical and Biological Setting

[6] The temporal and spatial variability of the surface ocean *p*CO₂ on continental shelves are influenced by a combination of physical and biogeochemical factors, including surface temperature-driven solubility, biological processes, fall-to-winter vertical mixing, ocean circulation, river runoff, and shelf-ocean exchange [*Wang et al.*, 2013]. Here we provide a summary of the physical and biological factors that are potentially important in shaping the *p*CO₂ variability in the North American east coast continental shelf.

[7] The definition of the coastal ocean is elusive, as it can be related to bathymetry, hydrography, or distance from shore; and some features, such as river plumes and coastal biomass maxima, can be ephemeral. Community efforts to standardize this definition to a fixed distance from shore, such as *Hales et al.* [2008] as adopted by the Surface Ocean CO₂ Atlas (SOCAT; <http://www.socat.info/>), extend seaward from the North American continent beyond what we feel represents the reach of coastal processes. As a result, we have used the outer boundaries of the regions defined by *Hofmann et al.* [2008, 2011] to define the extent of the coastal ocean. The North American east coast (Figure 1) encompasses three large regions of diverse physical and biological characteristics: the southeast U.S. continental shelf, also known as the South Atlantic Bight (SAB), the northeast U.S. continental shelf, and the Scotian Shelf (SS). Within the northeast U.S. continental shelf there are four subregions: the Middle Atlantic Bight (MAB), Georges Bank (GB), Nantucket Shoals (NS), and the Gulf of Maine (GoM). For this study, we combined the GB and NS regions into a single region (GB+NS) for simplicity and because these two regions share many similar physical and biogeochemical attributes [*Fox et al.*, 2005; *Shearman and Lentz*, 2004; *Thomas et al.*, 2003]. These North American continental shelf subregions are defined in *Hofmann et al.* [2011] with the GB+NS region separated from the GoM as in *Hofmann et al.* [2008]. The 58 coastal subregions shown in *Hofmann et al.* [2008] were developed based on a combination of bathymetry, SST fronts, stratification, and biological properties. For simplicity, here we consolidate the very fine regional domains into five major subregions described above. However, we recognize that previous studies have adopted other methods to identify regional domains [*Hales et al.*, 2008, 2012]. For example, a self-organizing mapping method has been adopted to subregionalize the North American Pacific Coast [*Hales et al.*, 2012]. The method relies on an artificial neural network to identify biogeochemical regions within the target study area.

[8] Our focus is on the continental shelf that we operationally define as depths less than 200 m since the depth of the actual shelf break varies. Bathymetric variation in our study area is large. Portions of GB and NS are only several

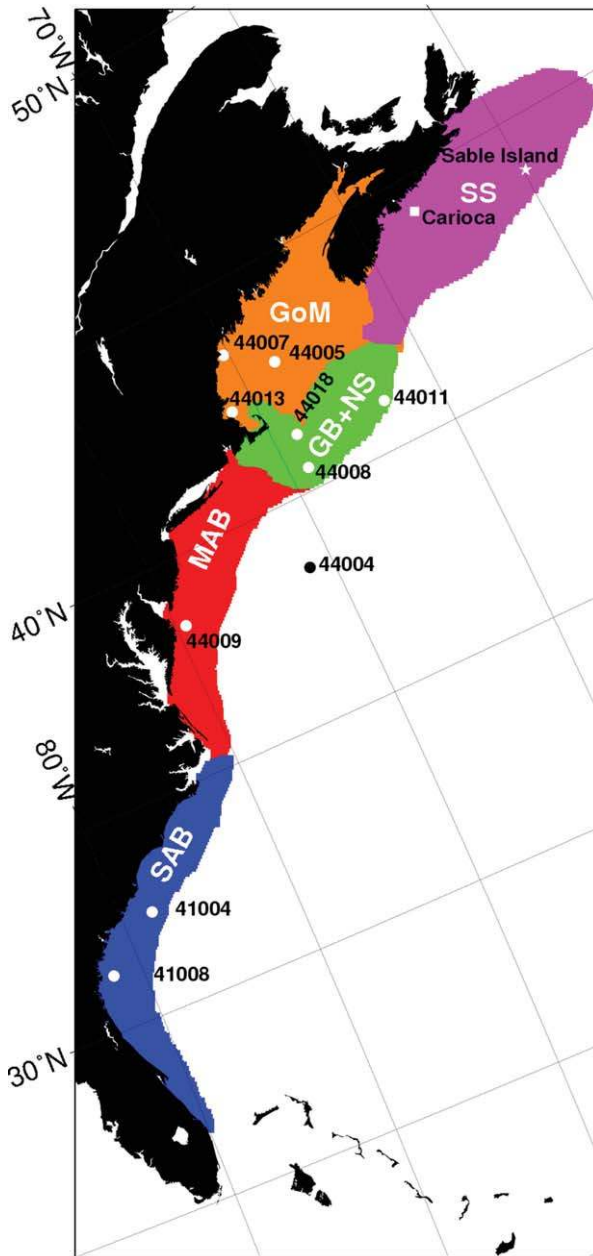


Figure 1. Regional domains for analysis adapted from Hofmann *et al.* [2008] and Hofmann *et al.* [2011]. The white circles show the locations of the NDBC buoys within each regional domain. The white star shows the location of the Sable Island meteorological station and the white square the location of the Carioca buoy.

meters below the sea surface, whereas in the GoM and areas of the SS, water depths exceed 200 m. Our study area is also at the “crossroads” of the north flowing Gulf Stream and the southwest flowing slope water-Labrador current [Rossby, 1987]. Chapman and Beardsley [1989] suggest that glacial melt and runoff from Western Greenland generates a buoyancy-driven coastal current that flows over the SS and GB and eventually into the MAB. This coastal current is an important driver to the distribution of the marine CO₂ system, including surface $p\text{CO}_2$ along its flow path

[Wang *et al.*, 2013], i.e., the Gulf of St Lawrence, the SS, the GoM, and the MAB. There is little exchange of water between the MAB and SAB along the narrow shelf at Cape Hatteras. In the SAB, the Gulf Stream is close to the shelf break and has a direct influence on the outer SAB shelf [Signorini and McClain, 2007], readily identifiable by the warm and salty signature shown in seasonal maps of sea surface temperature (SST), sea surface salinity (SSS), and chlorophyll (*Chl*) of Figure 2 (see section 3 for methodology), whereas north of Cape Hatteras, the influence of the Gulf Stream is more indirect. Here anticyclonic warm core rings result from landward meanders of the Gulf Stream [Joyce *et al.*, 1992]. The rings are carried in the southwestward flow of slope water where they interact with the outer shelf from GB to Cape Hatteras, frequently entraining phytoplankton-rich shelf water [Joyce *et al.*, 1992]. Near Cape Hatteras, the warm core rings may be reabsorbed into the Gulf Stream, a process readily apparent in daily time series animations of chlorophyll (*Chl*) and SST. In the SAB, the outer shelf waters are warmer (Figure 2) in summer and autumn than winter and spring due, in part, to the proximity of the Gulf Stream as a result of the expansion of the subtropical gyre [Signorini and McClain, 2007].

[9] The $p\text{CO}_2$ variability in riverine-plume systems is a result of complex biogeochemical interactions. In the Gulf of Maine for instance, labile riverine carbon is responsible for sustaining supersaturated $p\text{CO}_2$ conditions in late fall, while at other times of the year phytoplankton productivity, most likely driven by inputs of riverine dissolved inorganic nitrogen, is responsible for $p\text{CO}_2$ undersaturation [Salisbury *et al.*, 2008]. The North American east coast continental shelf is influenced by the discharge of several major rivers and estuaries (Chesapeake Bay, Delaware Bay, and Gulf of St Lawrence, for example) that contribute to complex physical and biogeochemical interactions that influence the seasonal and interannual variability of the surface ocean $p\text{CO}_2$, an important parameter for the determination of the sea-air CO₂ flux. Vandemark *et al.* [2011] showed that the observed $p\text{CO}_2$ and CO₂ flux dynamics in the Gulf of Maine are dominated by a seasonal cycle, with a large spring influx of CO₂ and fall-to-winter efflux back to the atmosphere. They also showed that in the western Gulf of Maine the ocean is a net source of carbon to the atmosphere ($+0.38 \text{ mol CO}_2 \text{ m}^{-2} \text{ yr}^{-1}$) over a period of 5 years, but with a moderate interannual variation where years 2005 and 2007 represent cases of regional source ($+0.71 \text{ mol CO}_2 \text{ m}^{-2} \text{ yr}^{-1}$) and sink ($-0.11 \text{ mol CO}_2 \text{ m}^{-2} \text{ yr}^{-1}$) anomalies, respectively. Comparison of results with the neighboring Middle Atlantic and South Atlantic Bight shelf systems showed that the Gulf of Maine differs by enhanced $p\text{CO}_2$ control factors other than temperature-driven solubility, such as biological drawdown, fall-to-winter vertical mixing, and river runoff [Salisbury *et al.*, 2008; Shadwick *et al.*, 2010].

[10] Shadwick *et al.* [2011] investigated the seasonal variability of $p\text{CO}_2$ in the Scotian Shelf and concluded that the region acts as a net source of CO₂ to the atmosphere on an annual basis ($1.4 \text{ mol CO}_2 \text{ m}^{-2} \text{ yr}^{-1}$). On a seasonal basis, there is a reversal of the flux only when a pronounced undersaturation of surface waters is reached for a short period during the spring bloom. Outside of the spring bloom period, the competing effects of temperature and biology

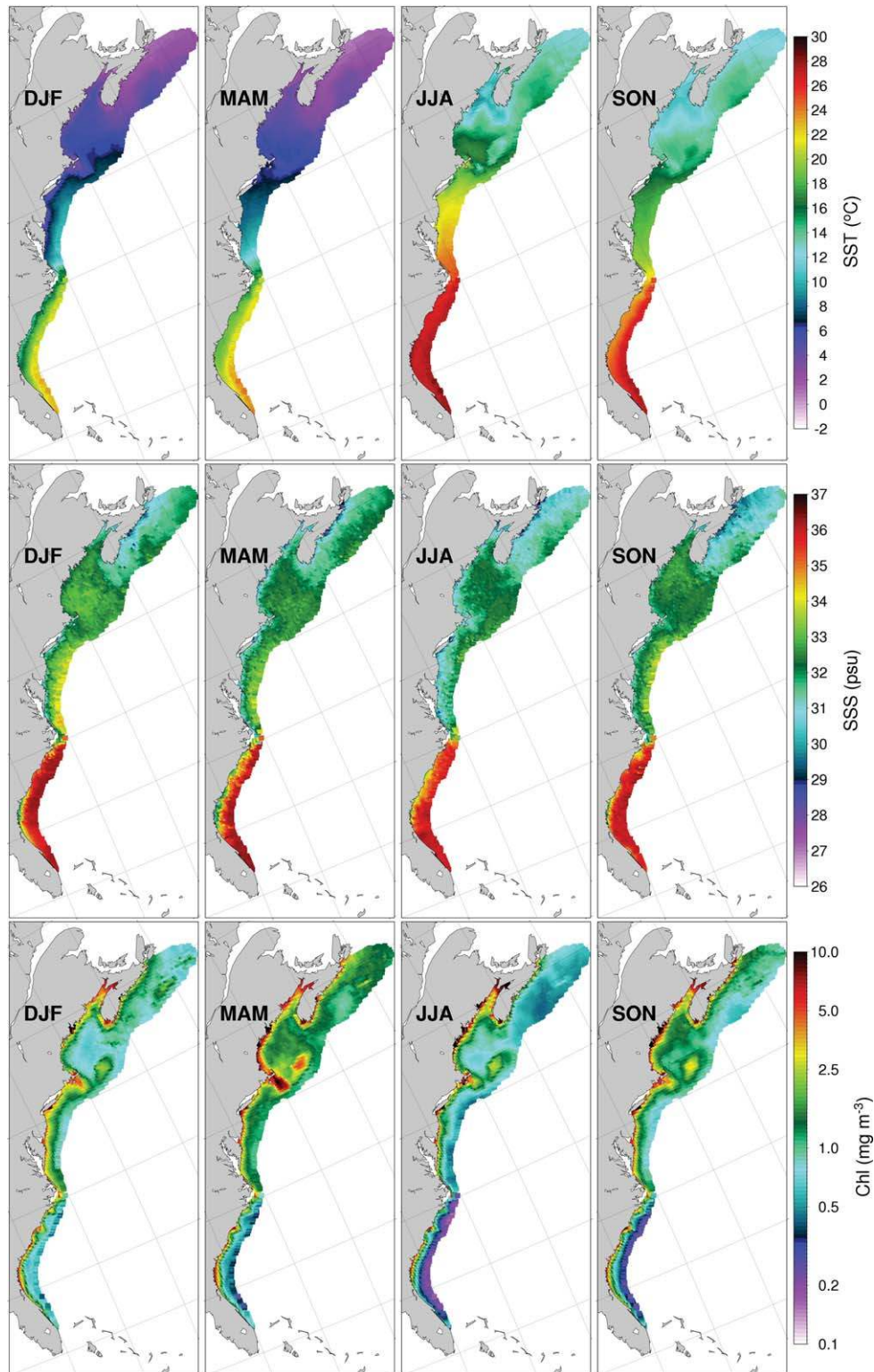


Figure 2. Seasonal climatology maps of SST, SSS, and *Chl*. Upper row: SST composites from MODIS Aqua; middle row: SSS composites from World Ocean Data 2009; bottom row: *Chl* composites from MODIS Aqua. Refer to section 3 for details. The MODIS SST and *Chl* seasonal climatologies are based on the period 2002–2011. The seasons are defined as Dec-Jan-Feb (DJF), Mar-Apr-May (MAM), Jun-Jul-Aug (JJA), and Sep-Oct-Nov (SON).

influence on surface $p\text{CO}_2$ are nearly equal and opposite. *DeGrandpre et al.* [2002], based on measurements of surface ocean $p\text{CO}_2$ during the Ocean Margins Program

[*Verity et al.*, 2002], concluded that the MAB is a sink of atmospheric CO_2 with an annual mean of $-1.0 \pm 0.6 \text{ Tg C yr}^{-1}$, or an area average of $-1.1 \pm 0.7 \text{ mol CO}_2 \text{ m}^{-2} \text{ yr}^{-1}$.

A significant portion of this atmospheric uptake is a result of the annual cycle of heating and cooling combined with strong winds during the winter undersaturation period.

[11] *Jiang et al.* [2008] showed that on an annual basis the SAB is a relatively small net sink of atmospheric CO₂ (-0.48 ± 0.21 mol CO₂ m⁻² yr⁻¹). Seasonally, the SAB shifts from a sink of atmospheric CO₂ in winter to a source in summer. The annual cycle of sea surface temperature plays an important role in controlling the seasonal variation of *p*CO₂. The combination of stronger wind speeds during fall winter, when CO₂ undersaturation is significant due to lower SSTs, results in a net annual CO₂ sink. Other important factors controlling the *p*CO₂ variability in the SAB are the marsh export of organic carbon and dissolved inorganic carbon (DIC) in the warm months (June–November), which directly supports CO₂ outgassing in these months via organic carbon decomposition and increase in DIC [*Jiang et al.*, 2013; *Wang et al.*, 2005]. In addition, the marsh areas in the SAB also export alkalinity, another important factor influencing the variability of *p*CO₂ and sea-air flux [*Wang et al.*, 2005; *Wang and Cai*, 2004].

[12] The seasonal *Chl* climatology from MODIS Aqua (Figure 2) shows that the maximum *Chl* in the GoM, GB, and NS occurs during spring (March–April–May, MAM). The GB region has the highest *Chl* in spring, but it is maintained at concentrations above 2.5 mg m⁻³ in all seasons due to vigorous tidal mixing. Figure 2 also shows that the low-salinity nearshore waters along the entire east coast coincide with regions of elevated *Chl*, an indication of the influence of nutrient-rich riverine waters. On the MAB shelf, there is a high-*Chl* region during winter (December–January–February, DJF) in the nearshore and outer-shelf waters, but the fall bloom (SON) dominates between approximately the 40 and 60 m isobaths. The high satellite-derived “*Chl*” in winter may be in part colored dissolved organic matter flowing out from rivers, plus photoacclimation by phytoplankton (higher *Chl-a* due to low surface solar radiation and a well-mixed water column).

[13] The minimum surface *Chl* over much of the MAB occurs during summer (JJA) when highest SST (Figure 2), peak stratification and a pronounced subsurface *Chl* maximum layer occur [*O’Reilly and Zetlin*, 1998]. Summer mixed-layer depths of ~3.5 to 10 m are typical for MAB shelf waters. The spring bloom (MAM) is clearly shown by the elevated *Chl* concentrations in the MAB, GB, and GoM (Figure 2). Figure 2 also shows that the SAB *Chl* has its largest changes in the outer shelf, with a maximum in DJF and lowest values in JJA under the influence of the oligotrophic waters of the Gulf Stream.

3. Data Sets and Methods

3.1. Processing of In Situ and Satellite Data Sets

[14] The surface ocean *p*CO₂ data are obtained from SOCAT, combined with additional available data from regionally specific field experiments (see Appendix A) and binned by month for each year (1978–2010) into 0.15° × 0.15° grid cells. The SOCAT data [*Pfeil et al.*, 2012] holds 6.3 million quality-controlled surface ocean *p*CO₂ from the global oceans and coastal seas covering the period of 1968–2007. These data were put together following uniform format and a strict protocol that included quality con-

trol with clearly defined criteria performed by a team of international experts.

[15] The MatLab function *bin2d*, developed by *J. Nielsen* and available at the Nansen Environmental and Remote Sensing Center (NERSC) from www-2.nersc.no/~even/, was used to bin all data sets into the study grid. First, all the available data within 24°N to 46°N and 82°W to 56°W were selected for binning. These included 416,261 collocated surface ocean *p*CO₂, SST, and sea surface salinity (SSS) values from SOCAT from the period 1978–2007, 11,628 from the 2006 SAB cruise (only 2005 cruises are included in SOCAT), and 309,665 from the GoM (2004–2010). The binned *p*CO₂ data were then adjusted to reference year 2004 using an atmospheric growth rate of 1.68 μatm yr⁻¹ [*Le Quéré et al.*, 2010] and assuming that the surface ocean *p*CO₂ is trending at the same pace as the atmosphere. All the adjusted *p*CO₂ data were then binned into 12 individual calendar months, each containing the average of all data within a particular month and grid bin. The data were then divided into regional study domains following the boundaries shown in Figure 1.

[16] The available *p*CO₂ data were divided into two individual sets, one dedicated to algorithm development (data bins covering more than 6 months) and one dedicated to algorithm evaluation (data bins covering less than 6 months). Surface ocean *p*CO₂ data from underway (UW) transects across the Scotian Shelf and *p*CO₂ time series from the CARIOCA buoy located at 44.296°N and 63.257°W [*Shadwick et al.*, 2010] were also used for algorithm evaluation, together with SOCAT data on the Scotian Shelf not used for the algorithm development. Figure 3a shows color-coded SOCAT surface ocean *p*CO₂ cruise tracks and Figure 3b shows corresponding coastal binned data with associated color-coded temporal coverage in months. The highest temporal coverage corresponds to the most traveled routes (in orange to red), i.e., most frequent destination ports (Boston, New York, Norfolk, Miami) used by the Volunteering Observing Ships (VOSs). The VOS ships according to map available at the CDIAC web site (http://cdiac.ornl.gov/oceans/VOS_Program/) are: the Skogafoss, A. Companion, Oleander, Falstaff, and Explorer of the Seas. The SOCAT data set also includes transects occupied by research vessels. Figure 3 clearly shows that the surface ocean *p*CO₂ data have spatial and temporal distribution gaps that may be potentially responsible for biases in the calculation of sea-air fluxes.

[17] Monthly sea-surface salinity (SSS) climatology was interpolated and gridded onto the 0.15° × 0.15° study domain grid using the World Ocean Database (WOD) 2009 station data and the method of Kriging. The Interactive Data Language (IDL) function KRIG2D was used for this purpose. Monthly climatologic mixed layer depth (MLD) was derived from WOD 2005 for the entire East Coast based on temperature profiles using 0.5°C temperature difference criterion [*Hofmann et al.*, 2008]. The MLD data were binned into the same 0.15° × 0.15° study domain grid.

[18] Both data and algorithm sea-air CO₂ flux estimates were obtained using gridded (0.25° × 0.25°) winds from the Jet Propulsion Laboratory Cross-Calibrated Multiple Platforms (CCMP) [*Atlas et al.*, 2011] product (<ftp://podaac-ftp.jpl.nasa.gov/allData/ccmp/L2.5/flk>). Monthly

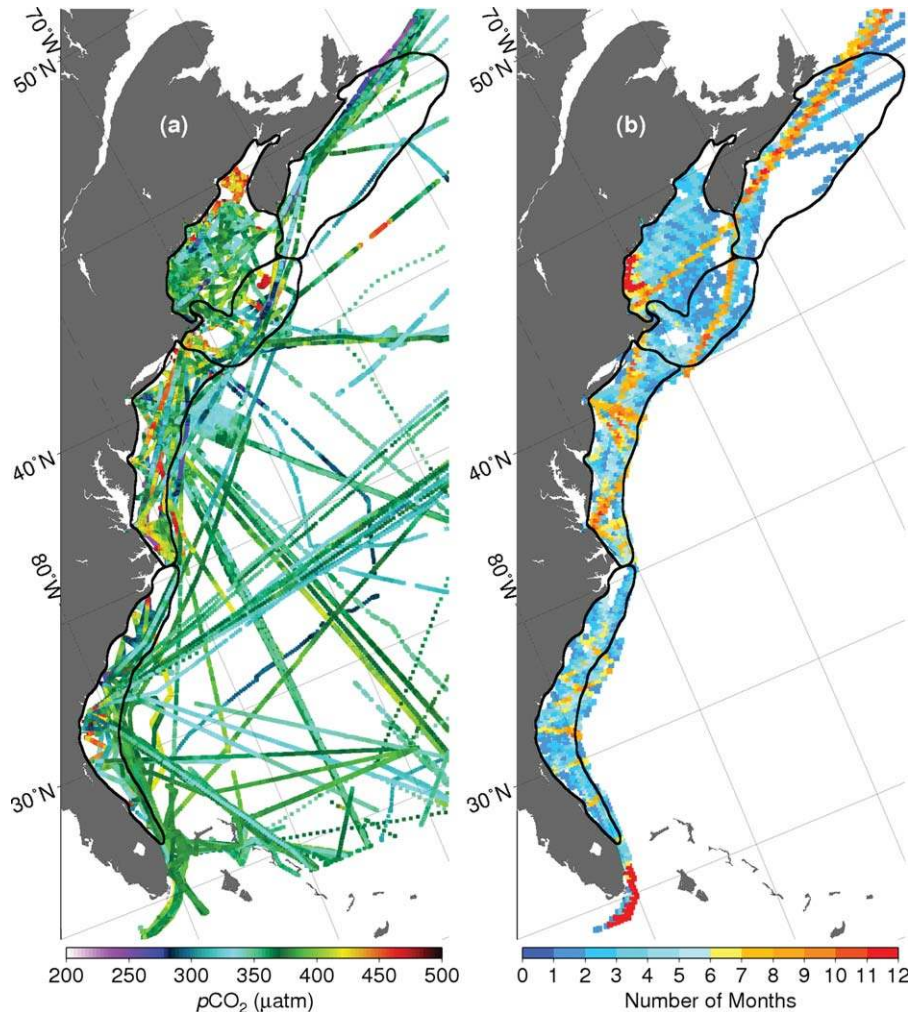


Figure 3. (a) Color-coded SOCAT surface ocean $p\text{CO}_2$ cruise tracks and (b) corresponding coastal binned data with associated color-coded temporal coverage in months. The highest temporal coverage corresponds to the most traveled routes (in orange to red), i.e., most frequent destination ports (Boston, New York, Norfolk, Miami) used by the Volunteering Observing Ships. The SOCAT data set also includes transects occupied by research vessels. The SS, GoM, GB+NS, MAB, and SAB regional boundaries are overlaid as black lines.

wind climatology was derived using data from 1999 to 2008, a period approximately centered on 2004, the reference year adopted for the adjusted surface ocean $p\text{CO}_2$ data. The climatologic and interannual CCMP monthly winds were regrided ($0.15^\circ \times 0.15^\circ$) and extrapolated nearshore using the function “surface” from Generic Mapping Tools (GMT) [Smith and Wessel, 1990; Wessel and Smith, 1991], which is based on an adjustable tension continuous curvature surface gridding method. High-frequency (10 min) winds from 10 NOAA National Oceanographic Data Center NDBC buoys (<http://www.nodc.noaa.gov/BUOY/>) and hourly winds from Sable Island were used to obtain correction coefficients to account for nonlinearities in the gas exchange parameterization resulting from the use of monthly climatologic winds. The method for deriving these coefficients is described under section 3.3.

[19] All parameters used to develop the $p\text{CO}_2$ algorithm and to derive the sea-air CO₂ flux, including all satellite

data products (SST and *Chl*), SSS, and the CCMP wind speed, were also binned monthly into the same grid. The satellite data products consisted of 9 km, level 3 mapped, MODIS Aqua (MODISA) climatologic and interannual monthly composites of SST and *Chl* obtained from the NASA ocean color distribution archive (<http://oceancolor.gsfc.nasa.gov/>). A validation between log-transformed MODISA *Chl* retrievals versus all available in situ observations (SAB to GoM, depth ≤ 200 m, $N = 404$), conducted using the SeaBASS (SeaWiFS Bio-optical Archive and Storage System: <http://seabass.gsfc.nasa.gov/>) data search and validation tools, showed good matchup agreement ($r^2 = 0.75$, RMSE = 0.30, APD = 35.8%). For the algorithm development, we used the available binned surface ocean $p\text{CO}_2$, SST, and SSS derived from the in situ data, combined with monthly climatologic satellite *Chl* binned at the same grid points as no in situ concurrent *Chl* measurements are available. For the algorithm application, we used

monthly interannual (2003–2010) satellite SST and *Chl*, and monthly climatologic SSS derived from WOD 2005 data.

[20] Seasonal maps were constructed by averaging the monthly data and derived products into four 3 month composites, defined as: winter (December-January-February, DJF), spring (March-April-May, MAM), summer (June-July-August, JJA), and autumn (September-October-November, SON).

3.2. Development of Regional *p*CO₂ Algorithms

[21] The algorithm development is based on binned in situ *p*CO₂, SST, and SSS, and satellite-derived *Chl* monthly climatology, as well as day of the year (Julian day). The algorithm was developed through the multiple linear regression (MLR) analysis based on all spatial bins containing more than six available monthly occurrences of the in situ data (remaining data were reserved for evaluation), and is represented as

$$pCO_2 = [a + bDay' + c(T - T_o) + d(S - S_o) + e[\log_{10}(Chl) - \log_{10}(Chl_o)] + 1.68(year - 2004)] \quad (1)$$

$$\text{where } Day' = \cos\left(\frac{2\pi(Day - \gamma)}{365}\right)$$

[22] The first terms in brackets represent the surface ocean *p*CO₂ corrected to the year 2004 and the last term is a correction factor for different years to account for the rise of surface ocean *p*CO₂ due to the uptake of anthropogenic CO₂. The input for “Day” (Julian day) was normalized sinusoidally (*Day'*) to emphasize the seasonal cycle and to allow January to be close to both February and December [Friedrich and Oschlies, 2009; Lefèvre et al., 2005]. The value of γ (phase of *Day'* in days) is optimized via iteration (ranging from 0 to 365 days) until the minimum RMSE is obtained. T_o , S_o , Chl_o are temperature, salinity, and chlorophyll mean values for each region. The choice of $\log_{10}(Chl)$ instead of *Chl* in our algorithm was an arbitrary choice, and therefore limited mechanistic information can be drawn in the empirical result.

[23] A separate analysis was conducted to evaluate the algorithm by using surface ocean *p*CO₂ data not used in the development of the algorithm equations (see section 4.1). These data consisted of bins from the monthly composites that have less than 6 months of available *p*CO₂ occurrences. Satellite-derived SST, *Chl*, in situ SSS monthly climatology was matched with the locations and months of the selected *p*CO₂ bins and used as algorithm input. The *p*CO₂ derived from the algorithm (*p*CO₂^{fit}) was matched with the observed *p*CO₂ (*p*CO₂^{obs}) and a scatterplot and histogram of residuals were made for all combined regions to evaluate the algorithm performance. The algorithm was also evaluated using data from the SS [Shadwick et al., 2010].

3.3. Calculation of the Sea-Air CO₂ Flux

[24] The air minus sea *p*CO₂ difference (ΔpCO_2) was calculated using monthly GLOBALVIEW [GLOBALVIEW-CO₂, 2011] atmospheric *x*CO₂ from Grifton, North Carolina, a station located approximately midway in the study domain. The *x*CO₂ (in $\mu\text{mol mol}^{-1}$) was converted to

*p*CO₂ (air) using the method of Jiang et al. [2008]. For this conversion, we used monthly surface barometric pressure and air temperature from NOAA NCEP-NACR CDAS-1 [Kalnay et al., 1996] and monthly climatologic SSS from WOA09. Although several other GLOBALVIEW stations are available along the study coastal domain, the atmospheric *p*CO₂ records are not very different to justify a more site-specific use of the data. Regarding the use of the atmospheric *x*CO₂ in this study, it has been demonstrated that there are uncertainties involved in using marine boundary layer *x*CO₂ rather than the in situ *x*CO₂ due to the effect of continental processes. For example, Jiang et al. [2008] showed that the average atmospheric *x*CO₂ on the SAB can be almost 10 ppm higher than the measured in the open ocean with the potential of reversing the direction of the sea-air flux. Although this is a potential source of uncertainty in the calculation of the sea-air flux, concurrent in situ atmospheric *x*CO₂ are only available for a limited number of coastal cruises.

[25] Climatologic (1999–2008) CCMP monthly wind speeds at 10 m anemometer height (U_{10}), based on a decade of data centered on the reference year 2004, were binned similarly and used to derive the monthly sea-air CO₂ flux for each bin and each month using the following gas transfer parameterization

$$\text{Flux} = k_{660} \left(\frac{Sc}{660}\right)^{-1/2} s \Delta pCO_2 \quad (2)$$

in units of mol CO₂ m⁻² d⁻¹. *Sc* is the Schmidt number (non dimensional), *s* the solubility of CO₂ in seawater in mol CO₂ m⁻³ μatm^{-1} , and ΔpCO_2 is the air minus sea *p*CO₂ difference in μatm . The term k_{660} is the quadratic gas transfer coefficient in cm h⁻¹ (converted to m d⁻¹). We calculated the sea-air CO₂ flux using two relationships of gas exchange with wind speed (U_{10}), the quadratic dependence formulation of Ho et al. [2011], for which $k_{660} = 0.262C_2U_{10}^2$, and the polynomial dependence of Wanninkhof et al. [2009], for which $k_{660} = 3 + 0.1U_{10} + 0.064C_2U_{10}^2 + 0.011C_3U_{10}^3$, using the appropriate nonlinearity correction coefficients C_2 and C_3 , which are correction factors to account for the use of monthly climatologic wind speeds [Jiang et al., 2008]. These were calculated using 10 min wind speeds from 10 NDBC buoys distributed within the SAB, MAB, GB+NS, and GoM regions, and Sable Island 1 h wind speeds for the SS (see locations in Figure 1), and the correction factor equations given in Jiang et al. [2008], $C_2 = (\frac{1}{n} \sum_j U_j^2) / U_{mean}^2$ and $C_3 = (\frac{1}{n} \sum_j U_j^3) / U_{mean}^3$, where U_j is the high-frequency wind speed (m/s), U_{mean} is the monthly mean wind speed (m s⁻¹), and *n* is the number of available wind speeds in each month. The value of C_2 and C_3 were obtained for each site and month for the period 1999–2008. Monthly climatologic averages were calculated for each site and for each region. The values of C_2 range from 1.2 to 1.3, while those for C_3 range from 1.6 to 2.0. These values were then used to apply corrections to the gas transfer parameterizations when calculating the sea-air CO₂ flux. The same methodology was applied to derive data-based and algorithm-based sea-air fluxes. We use the atmospheric convention for the CO₂ flux, i.e., a negative flux is defined as a sink of atmospheric CO₂ by the ocean.

Table 1. Coefficients and Statistical Data for $p\text{CO}_2$ Algorithm (Equation (1))^a

Means and Coefficients	SAB	MAB	GB+NS	GoM	SS
T_o (°C)	23.21	15.27	11.27	10.29	7.34
S_o (psu)	35.38	31.64	32.19	31.41	30.58
γ (days)	123	218	359	343	27
Chl_o (mg m ⁻³)	1.09	1.54	1.62	2.94	1.24
a (μatm)	378.69 ± 1.76	360.07 ± 1.40	370.66 ± 1.84	373.06 ± 1.38	351.43 ± 0.90
b (μatm)	24.00 ± 2.05	7.03 ± 4.82	37.05 ± 2.63	39.43 ± 1.68	69.31 ± 2.39
c (μatm °C ⁻¹)	12.23 ± 0.36	5.20 ± 0.47	6.88 ± 0.40	1.65 ± 0.24	8.77 ± 0.26
d (μatm psu ⁻¹)	-22.49 ± 1.71	1.11 ± 0.61	-10.95 ± 2.33	-1.34 ± 0.83	1.44 ± 0.86
e (μatm/log ₁₀ (Chl))	30.25 ± 5.87	-14.99 ± 5.51	10.05 ± 7.67	-20.65 ± 3.83	-100.32 ± 4.66
r^2	0.82	0.55	0.60	0.42	0.74
RMSE (μatm)	26.7	36.9	32.2	34.6	22.4
N	356	997	356	847	684

^aThe multiple regression coefficients and their corresponding standard errors were obtained using the MatLab function “regstats” with t statistics.

[26] The regional algorithms (Table 1 and equation (1)) were used to derive values of surface ocean $p\text{CO}_2$ using MODIS Aqua monthly composites of SST and Chl for 2003–2010, and monthly SSS climatology. Gap filling of missing satellite data was done with monthly climatology composites for each of the input parameters. The sea-air CO₂ flux was then computed using interannual monthly CCMP winds and the gas transfer parameterization shown in equation (2).

3.4. Monthly Climatology of DIC and Alkalinity for $p\text{CO}_2$ Parameter Sensitivity

[27] The data sets used to generate monthly climatologies of DIC and alkalinity (Alk) include the MODIS SST monthly climatology, the Kriged monthly SSS climatology derived from WOA 2009 salinity data, and surface ocean $p\text{CO}_2$ from the algorithm. Monthly alkalinity was derived as a function of salinity from *Cai et al.* [2010] using SSS monthly climatology. DIC was then derived from alkalinity, SST, SSS, and monthly $p\text{CO}_2$ from the algorithm using CO2SYS (http://cdiac.ornl.gov/ftp/co2sys/CO2SYS_calc_MATLAB/), a MatLab program to calculate the state of the carbonate system. The input for CO2SYS consisted of alkalinity, DIC, SST, SSS, the choice of H_2CO_3 and HCO_3^- dissociation constants (K_1 , K_2) of “Mehrbach refit” [Dickson and Millero, 1987], the choice of HSO_4^- dissociation constant of “Dickson” [Dickson, 1990], and zero concentration for silicate and phosphate. The total borate-salinity relationship of *Uppstrom* [1974] was used.

[28] The monthly binned SST, SSS, DIC, and alkalinity fields were then averaged over each region to obtain 12 monthly values for each variable and region. We refer to these regional averages as SST^i , SSS^i , DIC^i , and Alk^i , where the superscript indicates the calendar month from 1 to 12. We also computed the annual average of each of these four spatial averages, which we call, $\overline{\text{SST}}$, $\overline{\text{SSS}}$, $\overline{\text{DIC}}$, and $\overline{\text{Alk}}$. From the regional averages, we computed the monthly $p\text{CO}_2$ using CO2SYS,

$$p\text{CO}_2^i = p\text{CO}_2 (\text{SST}^i, \text{SSS}^i, \text{DIC}^i, \text{Alk}^i), \quad (3)$$

and the annual average, $\overline{p\text{CO}_2}$.

[29] The deviation of $p\text{CO}_2$ from its annual average is given by

$$\delta^i = p\text{CO}_2^i - \overline{p\text{CO}_2} \quad (4)$$

[30] To determine the sensitivity of $p\text{CO}_2$ to each of the four variables, we hold three variables at their annual averages and let the fourth variable change from month to month. For example, to determine the impact of temperature on $p\text{CO}_2$, we computed

$$p\text{CO}_2^{i,\text{SST}} = p\text{CO}_2 (\text{SST}^i, \overline{\text{SSS}}, \overline{\text{DIC}}, \overline{\text{Alk}}) \quad (5)$$

[31] In an analogous way, we computed $p\text{CO}_2^{i,\text{SSS}}$, $p\text{CO}_2^{i,\text{DIC}}$, and $p\text{CO}_2^{i,\text{Alk}}$, which describe the respective influences of SSS, DIC, and Alk on $p\text{CO}_2$. We also computed the deviation of $p\text{CO}_2$ from its annual average due to each of the four variables. For example, the deviation of $p\text{CO}_2$ from its annual average due to temperature is $\delta^{i,\text{SST}} = p\text{CO}_2^{i,\text{SST}} - \overline{p\text{CO}_2}$. Similarly, $\delta^{i,\text{SSS}}$, $\delta^{i,\text{DIC}}$, and $\delta^{i,\text{Alk}}$, describe the deviations of $p\text{CO}_2$ from its annual average due, respectively, to SSS, DIC, and Alk. The results of this analysis will be discussed in section 4.3.

4. Results and Discussion

[32] Regional algorithms were developed with distinct coefficients derived for each of the five regions (Table 1) and then used to derive seasonal and interannual surface ocean $p\text{CO}_2$ and sea-air CO₂ fluxes (Tables 2 and 3).

4.1. Performance of Regional Algorithms

[33] In this section, we provide an assessment of the statistical importance of each proxy parameter used in the algorithm (Figure 4), regional matchups of algorithm versus data and seasonal $p\text{CO}_2$ plots based on monthly averages derived from data and algorithm (Figure 5), algorithm versus data matchups using $p\text{CO}_2$ observations not used in the algorithm development (Figure 6), a regional matchup analysis for the Scotian Shelf (SS) using a combination of UW $p\text{CO}_2$ data from Dalhousie University and a few from SOCAT (Figure 7), and time series of algorithm $p\text{CO}_2$ for seven distinct subregions of the SS (concurrent data points) following a more recent work of *Thomas et al.* [2012] (Figure 8). Finally, a high-frequency algorithm validation was performed against surface $p\text{CO}_2$ observations from the CARIOCA buoy on the SS using concurrent hourly observations of SST, SSS, and Chl (Figure 9).

Table 2. Sea-Air CO₂ Flux for Reference Year 2004 From Binned Data, Algorithm for Year 2004, and Previous Studies (Literature)^a

Region	Area (1010 m ²)	Data (mol CO ₂ m ⁻² yr ⁻¹ / Tg C yr ⁻¹)		Algorithm (mol CO ₂ m ⁻² yr ⁻¹ / Tg C yr ⁻¹)		Literature (mol CO ₂ m ⁻² yr ⁻¹ /Tg C yr ⁻¹)
		k_{660}^1	k_{660}^2	k_{660}^1	k_{660}^2	
SS	12.82	-1.10 ± 0.25	-1.21 ± 0.27	-0.39 ± 0.34	-0.42 ± 0.36	+1.42 ± 0.28 ^b
		-1.69 ± 0.39	-1.87 ± 0.42	-0.56 ± 0.50	-0.60 ± 0.53	+2.19 ± 0.43
GoM	12.77	+0.11 ± 0.21	+0.04 ± 0.22	+0.01 ± 0.08	+0.01 ± 0.08	+0.38 ± 0.26 ^c
		+0.17 ± 0.32	+0.06 ± 0.34	+0.02 ± 0.12	+0.02 ± 0.12	+0.58 ± 0.40
GB+NS	5.83	-0.65 ± 0.20	-0.71 ± 0.22	-1.27 ± 0.23	-1.37 ± 0.24	
MAB	9.31	-0.46 ± 0.14	-0.50 ± 0.15	-0.79 ± 0.16	-0.86 ± 0.16	
		-0.95 ± 0.24	-1.07 ± 0.27	-1.58 ± 0.19	-1.78 ± 0.19	-1.1 ± 0.7
SAB	10.20	-1.06 ± 0.27	-1.12 ± 0.30	-1.63 ± 0.21	-1.83 ± 0.22	-1.0 ± 0.6 ^d
		-0.79 ± 0.26	-0.68 ± 0.24	-0.61 ± 0.17	-0.67 ± 0.16	-0.48 ± 0.21 ^e
Total	50.63	-0.97 ± 0.31	-0.83 ± 0.29	-0.67 ± 0.20	-0.74 ± 0.20	-0.59 ± 0.26
		-4.01 ± 0.30	-4.26 ± 0.31	-3.63 ± 0.24	-4.01 ± 0.25	

^aUncertainties (ϵ) for the estimates from the data were obtained as $\epsilon = STD/\sqrt{N}$, where STD is the standard deviation and N the number of data points. Uncertainties for the sea-air CO₂ flux estimates from the algorithm were based on the standard deviation of all monthly estimates for the period 2003–2010. Both specific (mol CO₂ m⁻² yr⁻¹) and total (Tg C yr⁻¹) sea-air fluxes are shown for each region and total for the whole coast. Two gas transfer coefficients were used, the polynomial equation of Wanninkhof *et al.* [2009] (k_{660}^1) and the quadratic dependence version of Ho *et al.* [2011] (k_{660}^2) adjusted for steady winds using the nonlinearity coefficients C_2 and C_3 . Negative sign represents ocean uptake.

^bShadwick *et al.* [2011].

^cVandemark *et al.* [2011] is 5 year mean (2004–2208) but ranging from +0.71 (2005) to -0.11 (2007) mol m⁻² yr⁻¹.

^dDeGrandpre *et al.* [2002].

^eJiang *et al.* [2008]. Values for footnote e, c, and b were converted from specific to total flux, or mol CO₂ m⁻² yr⁻¹ to Tg C yr⁻¹ ($\times 12 \times \text{area} \times 10^{-12}$). $k_{660}^1 = 3 + 0.1U_{10} + 0.064C_2U_{10}^2 + 0.011C_3U_{10}^3$ and $k_{660}^2 = 0.262C_2U_{10}^2$.

[34] Figure 4 shows the statistical (goodness-of-fit) performance resulting from the incremental addition of proxy parameters for each of the five regions. The statistical performance is shown as a goodness-of-fit diagram with normalized RMSE on the x axis, and $(1 - r^2)$ on the y axis. Consequently, a perfect fit would lie at the origin of this diagram (0, 0). The diagram shows that the variable Day' by itself provides $(1 - r^2)$ values less than 0.6 for all regions. Incremental improvements of both normalized RMSE and $(1 - r^2)$ are different for each region. Extreme examples of statistical improvement are the addition of salinity for the SAB and $\log_{10}(Chl)$ for the SS.

[35] Figure 5 shows scatterplots of algorithm-derived versus observed surface ocean $p\text{CO}_2$ and associated seasonal plots of regionally averaged $p\text{CO}_2$. As shown in Table 1, there is a statistical range for the coefficients derived for each region using equation (1). The r^2 is lowest for the GoM (0.42) and highest for the SAB (0.82). The quality of the statistical fit depends on a combination of factors, including data coverage and how well the proxy variables

represent the surface ocean $p\text{CO}_2$ variability in space and time within each region.

[36] The regional algorithms were then applied using binned inputs (SST, SSS, and Chl) matching the month and location of the observed surface ocean $p\text{CO}_2$ not used for the algorithm development, and then compared with the corresponding observed $p\text{CO}_2$. The results are shown in Figures 6a and 6b. The observed versus algorithm correlation coefficient (color-coded scatterplot in Figure 6a with summary of statistics in the legend) range from 0.27 (r^2) for the GoM with a RMSE = 25 μatm to 0.78 for the SAB with a RMSE = 21 μatm . The histogram of residuals (Figure 6b) shows that 86% of the residuals are less than the observed $p\text{CO}_2$ standard deviation ($\pm\sigma$), while 40% of residuals are within less than $\sigma/3$ ($\pm 16 \mu\text{atm}$).

[37] Data from SOCAT on the SS, and Dalhousie University UW transects [Shadwick *et al.*, 2010] covering the period of 2004–2008, were averaged within seven $2^\circ \times 2^\circ$ boxes on the SS (Figure 7a) and compared with area-averaged algorithm predictions within the same boxes. The

Table 3. Sea-Air CO₂ Flux Derived From the Regional Algorithms for 2003–2010^a

Year	SAB	MAB	GoM	GB+NS	SS	Sum
2003	-0.78/-0.90	-2.18/-2.43	+0.002/+0.009	-1.72/-1.20	-0.33/-0.55	-5.07
2004	-0.75/-0.88	-2.08/-2.31	+0.107/+0.166	-1.72/-1.20	-0.27/-0.39	-4.61
2005	-0.95/-1.12	-1.92/-2.13	+0.068/+0.108	-1.49/-1.04	+0.18/+0.15	-4.03
2006	-0.74/-0.88	-1.56/-1.73	-0.052/-0.074	-1.05/-0.73	-0.01/-0.02	-3.43
2007	-0.43/-0.51	-1.76/-1.95	-0.129/-0.191	-1.71/-1.20	-1.01/-1.55	-5.40
2008	-0.78/-0.93	-1.72/-1.91	-0.045/-0.062	-1.21/-0.85	-0.55/-0.77	-4.52
2009	-0.66/-0.76	-1.90/-2.11	-0.024/-0.028	-1.32/-0.92	-0.72/-1.14	-4.96
2010	-0.91/-1.08	-2.16/-2.41	+0.079/+0.126	-1.21/-0.85	-0.18/-0.40	-4.62
Mean	-0.89 ± 0.18	-2.12 ± 0.24	+0.007 ± 0.112	-1.00 ± 0.18	-0.58 ± 0.52	-4.58

^aThe flux is given in two different units for each year (mol CO₂ m⁻² yr⁻¹/Tg C yr⁻¹), and in Tg C yr⁻¹ for the overall 8 year mean and whole coast sum. The flux was calculated using the gas transfer equation of Ho *et al.* [2011]. Negative sign represents ocean uptake.

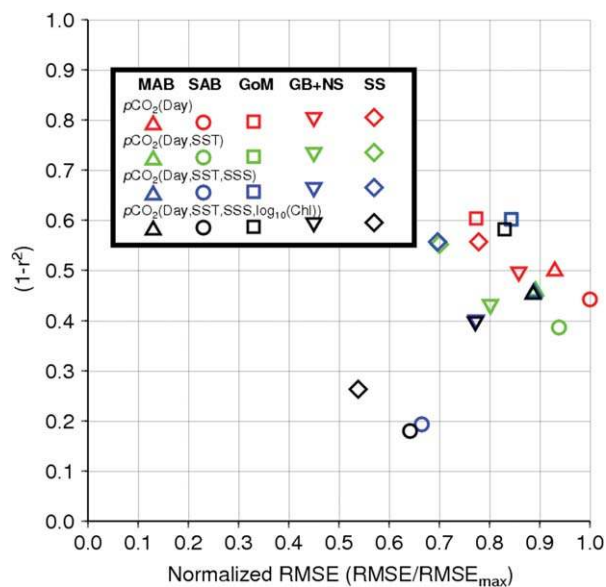


Figure 4. Plot of goodness-of-fit statistics for all regional MLRs with incremental addition of corresponding proxy parameters. The x axis shows the RMSE normalized by the maximum attained value among all MLRs, while the y axis shows $(1 - r^2)$. Thus, a perfect match between data and MR values would be centered at the origin (0, 0).

scatterplot of observed versus algorithm pCO_2 for the 37 resulting averages is shown in Figure 7b. The agreement between data and algorithm predictions is quite reasonable with $r^2 = 0.79$ and $RMSE = 26.2 \mu atm$. The time series of algorithm pCO_2 was obtained using SST and Chl from MODIS Aqua monthly composites and WOA09-derived SSS climatology. The algorithm time series for all seven boxes are shown in Figures 8a and 8b with the SOCAT (red circles) and UW (blue circles) values superposed for comparison. A high-frequency algorithm test was done by comparing the CARIOCA buoy 1 h pCO_2 record on the SS during 2007–2010 with algorithm results using 1 h inputs of SST, SSS, and calibrated fluorometer Chl concurrent observations from the buoy. These data have been reported by Thomas *et al.* [2012]. The time series and scatterplot of observed versus algorithm pCO_2 are shown in Figure 9. The algorithm predictions track the observed pCO_2 reasonably well with $r^2 = 0.46$, $RMSE = 40.3 \mu atm$ and mean absolute percent difference (MAPD) of 8.8%. The observed and algorithm values for 2007–2010 mean and standard deviation are quite similar, $422.3 \pm 54.7 \mu atm$ and $413.1 \pm 56.9 \mu atm$, respectively, which show a relatively small bias (9 μatm) and very similar variance.

4.2. Seasonal Surface Ocean pCO_2 , Alkalinity, DIC, and Sea-Air Flux From Data and Algorithm

[38] Figure 10 shows seasonal maps of algorithm surface ocean pCO_2 adjusted for reference year 2004 and corresponding seasonal maps of alkalinity and DIC. Figure 10 shows that the temporal and spatial variability of pCO_2 is quite different from region to region and that the seasonal changes are not in sync among the five analyzed coastal domains. This is also evident in the seasonal plots of data-derived surface ocean pCO_2 in Figure 5. The lowest values

(280–320 μatm) occur mostly during winter (DJF) in the MAB, SAB, and in the nearshore areas of the SS in spring (MAM). Low values are also present in spring in the GB+NS region. These low values are generally associated with low SSTs (see Figure 2). The highest values ($>480 \mu atm$) occur in the offshore region of the SS in autumn (SON) and the nearshore areas of the SAB in summer (JJA), the latter influenced by the discharge of carbon-rich (primarily DOC) estuarine effluents [Alberts and Takacs, 1999; Cai, 2011] and marsh DIC export [Wang and Cai, 2004]. The surface ocean pCO_2 in the MAB shows much less variability alongshore than cross-shelf, except in the southern region and outer shelf where Gulf Stream intrusions and shelf-slope fronts induce strong hydrographic and biogeochemical horizontal gradients. DeGrandpre *et al.* [2002], and references within, identified similar alongshore homogeneity in connection with little alongshore variability on midshelf hydrography, nutrients, surface-dissolved oxygen, Chl concentrations, and primary production. The high values in the offshore region of the SS in autumn are associated with low drawdown by phytoplankton, as indicated by the higher values of DIC, as shown in Figure 10 discussed later in this section, and confirmed by the work of Craig *et al.* [2013] for this region. The GoM has highest pCO_2 ($>400 \mu atm$) values in winter and fall when vertical mixing is more vigorous and phytoplankton drawdown is significantly reduced.

[39] The seasonal maps of alkalinity in Figure 10 follow the seasonal surface salinity distribution in Figure 2 as alkalinity was derived as a linear function of salinity, albeit with different coefficients for each region. There is a sharp transition in alkalinity at Cape Hatteras. South of it, in the SAB, alkalinity is highest in the middle and outer shelves due to the influence of high-salinity Gulf Stream waters. Alkalinity is highly reduced in the nearshore region under the influence of low-salinity riverine waters. However, in the very nearshore areas high alkalinity values were observed due to significant export from the marsh areas during the warm months [Cai *et al.*, 1998]. North of Cape Hatteras all regions have much lower alkalinity than the middle and outer shelf regions of the SAB. The inner and middle shelf regions of the MAB and southern GoM have even lower alkalinity, especially during summer (JJA) when surface salinity is at a minimum. This summer minimum salinity follows the peak discharge of the major rivers in spring with a delay of approximately 1–2 months [Whitney, 2010]. However, the SSS minimum on the SS comes in autumn (SON) with the peak St. Lawrence outflow.

[40] The Alk and salinity relationships generally followed a single river-ocean mixing line in the SAB and MAB regions, but a two-segment line in the northeastern waters due to the strong alongshore current and influences from the low alkalinity local rivers [Cai *et al.*, 2010].

[41] The seasonal DIC maps in Figure 10 show highest values in the GoM and offshore regions of the SS in winter-spring, a likely result of vigorous vertical mixing. Lowest DIC values occur in the MAB and southern GoM in summer, influenced by the low-DIC riverine waters that peak during spring, as well as low-DIC water of the Labrador Coastal Current that flows through the region [Wang *et al.*, 2013]. The DIC seasonal variability is also highly influenced by the drawdown of CO_2 by the net community

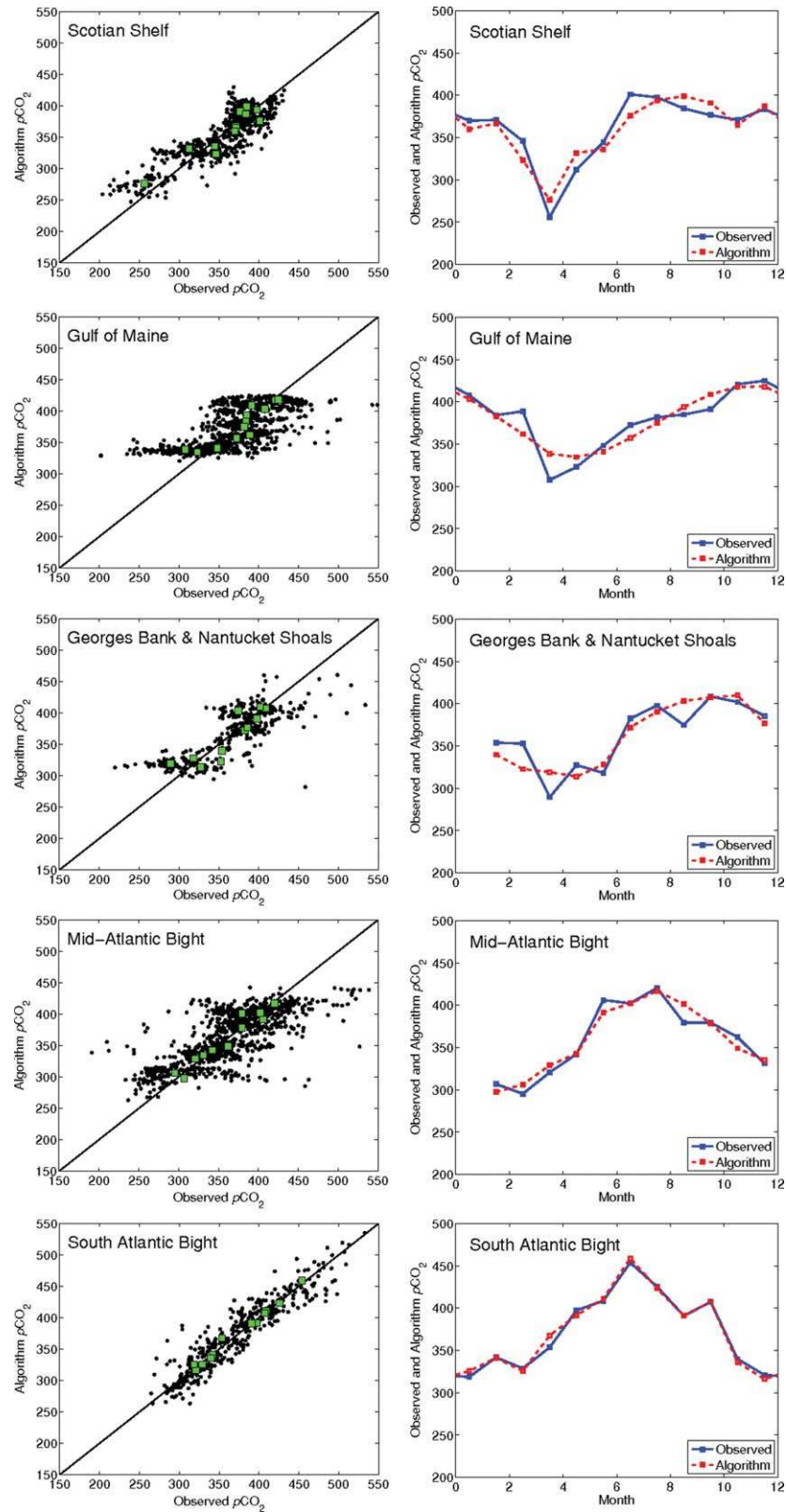


Figure 5. (top to bottom) scatterplots (left column) of observed (SOCAT) versus algorithm (equation (1)) $p\text{CO}_2$ (μatm) for the five regions (black dots all months, green squares monthly ensemble averages). The right column shows the mean seasonal plots of the ensemble averages for the equivalent regions. There are no data available for the MAB and GB+NS for January. Only data bins with more than 6 months of coverage were used.

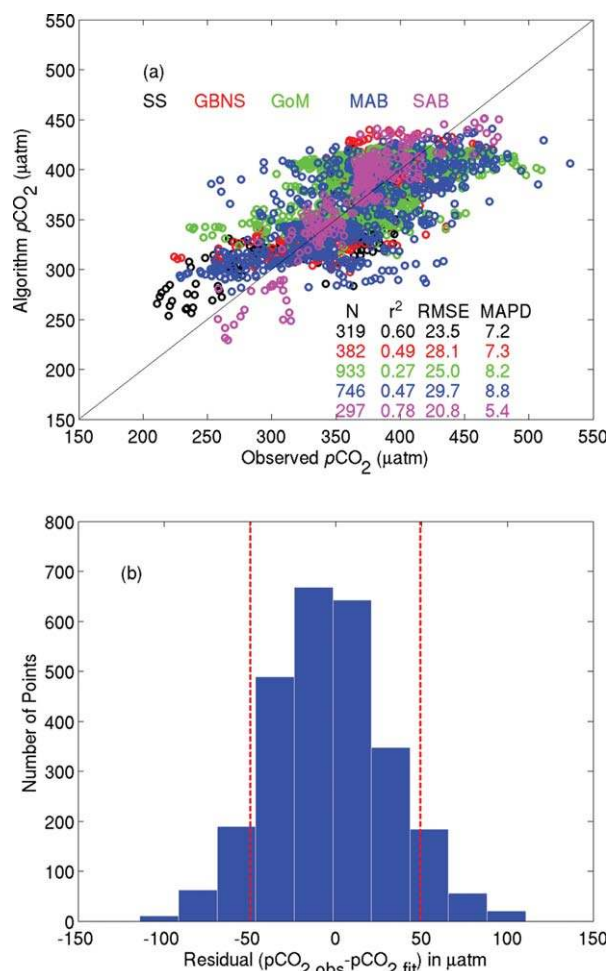


Figure 6. (a) Scatterplot of algorithm versus observed surface ocean $p\text{CO}_2$ based on observed values not used in the algorithm development (bins with temporal coverage less than 6 months). The r^2 , RMSE, and mean absolute percent difference (MAPD) are shown in the legend. (b) Histogram of residuals (observed minus algorithm). The red dashed vertical lines represent the standard deviation ($\pm\sigma$) of the observed $p\text{CO}_2$.

production during spring-summer. In general, the SAB has much less seasonal DIC and alkalinity variability than the other regions to the north.

[42] The monthly and annual mean sea-air CO₂ flux was calculated using $\Delta p\text{CO}_2$ derived from both binned data and algorithm (Table 2) and the two gas transfer parameterizations described in section 3.3. The estimates were based on monthly wind climatology for 1999–2008 derived from satellite (Atlas CCMP) winds. The differences between the two different parameterizations are relatively small ranging from 6% to 17%, except for the GoM where the fluxes are small causing much larger differences between the two methods. For simplicity, we compare the flux estimates between binned data and algorithm based on the *Ho et al.* [2011] parameterization.

[43] There is a general agreement in sign and magnitude between the data-derived and algorithm-derived estimates for the MAB, SAB, and GB+NS (Table 2). The annual mean sea-air CO₂ flux in the GoM derived by both methods

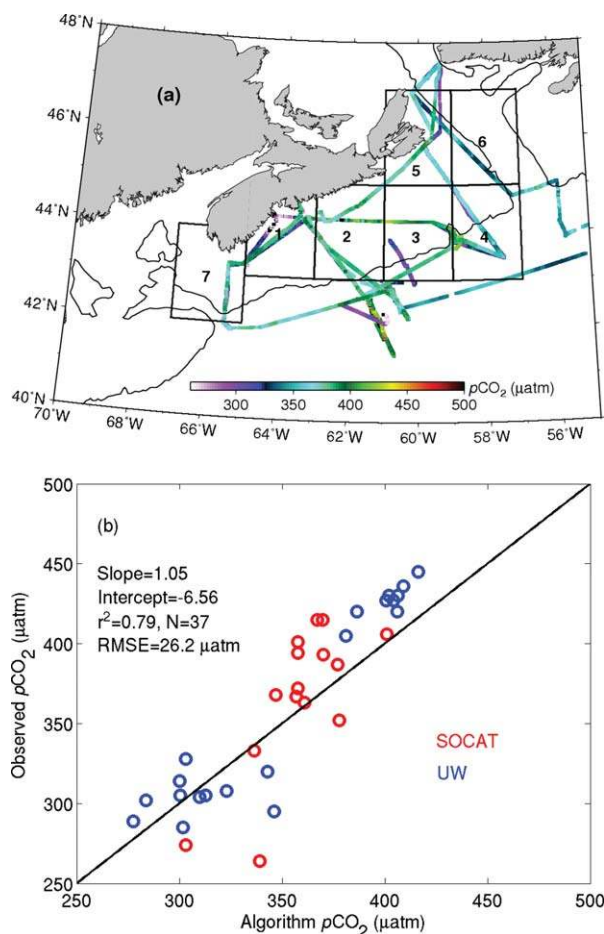


Figure 7. (a) Map showing the seven $2^\circ \times 2^\circ$ boxes covering the entire Scotian Shelf (SS) region adapted from *Shadwick et al.* [2010]. The contour line is the 200 m isobath. The algorithm and in situ (SOCAT (not shown) and UW observations from Dalhousie University cruises) mean surface ocean $p\text{CO}_2$ were obtained for each of the seven boxes for evaluation purposes. (b) The scatterplot of algorithm versus observed $p\text{CO}_2$ for all seven boxes is shown with corresponding statistics in the legend.

range from $+0.02 \pm 0.12$ to $+0.17 \pm 0.32 \text{ Tg C yr}^{-1}$, or a weak source to the atmosphere on average, but within the range of the estimates given by *Vandemark et al.* [2011] for the southern GoM (-0.16 to $+1.1 \text{ Tg C yr}^{-1}$ when converted from specific to upscaled total sea-air flux for the entire GoM). The MAB, SAB, GB+NS, and SS are net sinks ranging from -0.6 ± 0.2 to $-1.8 \pm 0.2 \text{ mol CO}_2 \text{ m}^{-2} \text{ yr}^{-1}$. These estimates from the binned data and algorithm are in general agreement with previous studies (see Table 2) when the range of uncertainty and interannual variability are taken into account. One exception is the SS where previous studies [*Shadwick et al.*, 2010, 2011] indicate that the SS is a source of CO₂ to the atmosphere while this study indicates the opposite. Since the algorithm seems to perform well in the SS when compared with the available data, the reason(s) for the apparent discrepancy remains elusive and highlights the fact that there are still large differences in the sea-air flux estimates with different degrees of uncertainty from region to region.

[44] The combined uptake by the east coast continental shelf based on both binned data and algorithm, and using both gas transfer parameterizations, ranges from 3.6 to 4.3 Tg C yr⁻¹.

4.3. Sensitivity Analysis of Parameters That Influence the *p*CO₂ Seasonal Variability

[45] Here we present a sensitivity analysis of the most influential parameters affecting the surface ocean *p*CO₂ vari-

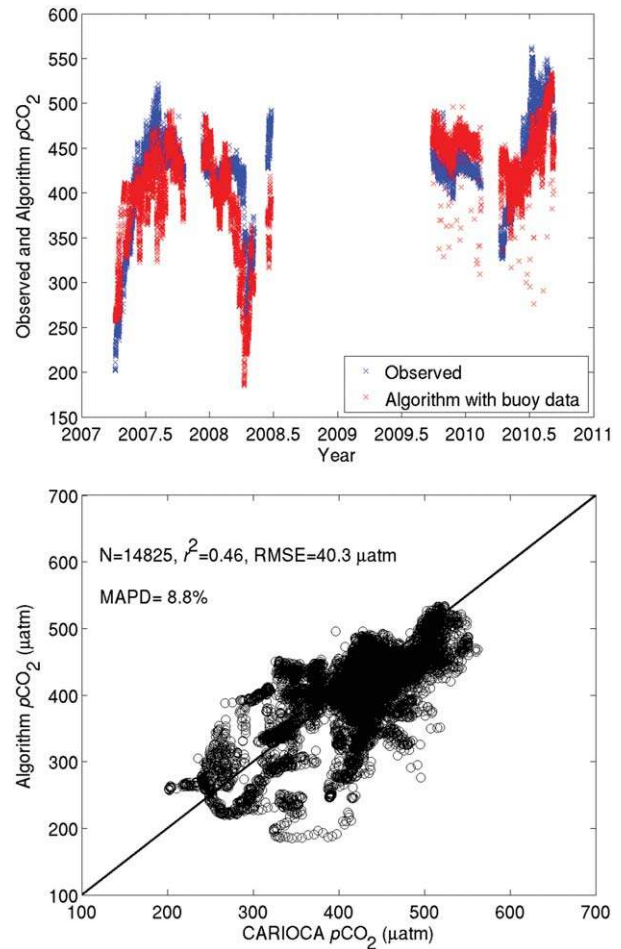
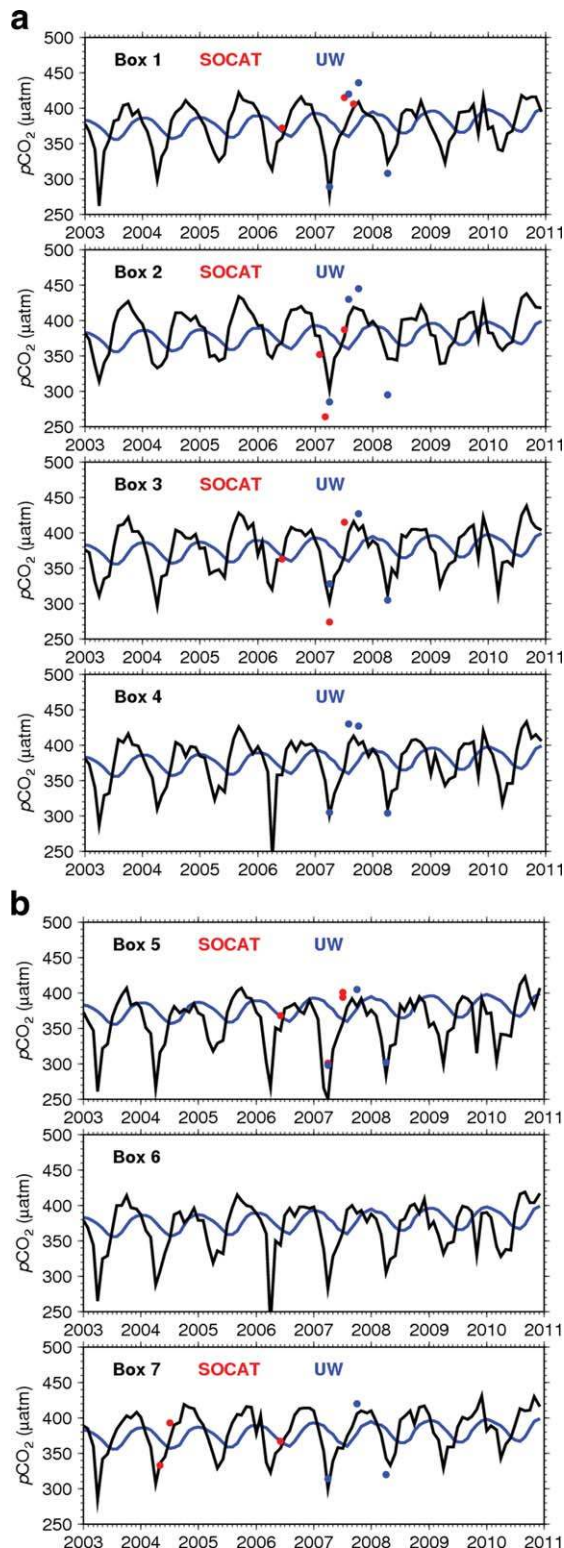


Figure 9. Time series of high-frequency (hourly) surface ocean *p*CO₂ measured (blue crosses) at the Carioca buoy from 2007 to 2010, and corresponding algorithm prediction (red crosses) using hourly values of SST, SSS, and calibrated fluorometer Chl as inputs (top). The scatterplot of observed versus algorithm *p*CO₂ is shown in the bottom.

ability in the study region. The seasonal cycles of each influential parameter are plotted in Figure 11 together with the seasonal surface ocean *p*CO₂ from the algorithm with the seasonal mean removed. Inspection of Figure 11 shows that the amplitude of SST and DIC contributions in the MAB, GoM, GB+NS, and SS are similar but having opposite phase. Seasonal variability of *p*CO₂ (DIC) in these regions is consistent with winter mixing enhancement and

Figure 8. (a) Time series of algorithm mean surface ocean *p*CO₂ (black lines) for boxes 1–4 shown in Figure 7a. The corresponding SOCAT (red dots) and Dalhousie UW (blue dots) data are shown for comparison. The blue lines are the atmospheric *p*CO₂. See Figure 7b for statistical evaluation. (b) Time series of algorithm mean surface ocean *p*CO₂ (black lines) for boxes 5–7 shown in Figure 7a. The corresponding SOCAT (red dots) and Dalhousie UW (blue dots) data are shown for comparison. The blue lines are the atmospheric *p*CO₂. See Figure 7b for statistical evaluation.

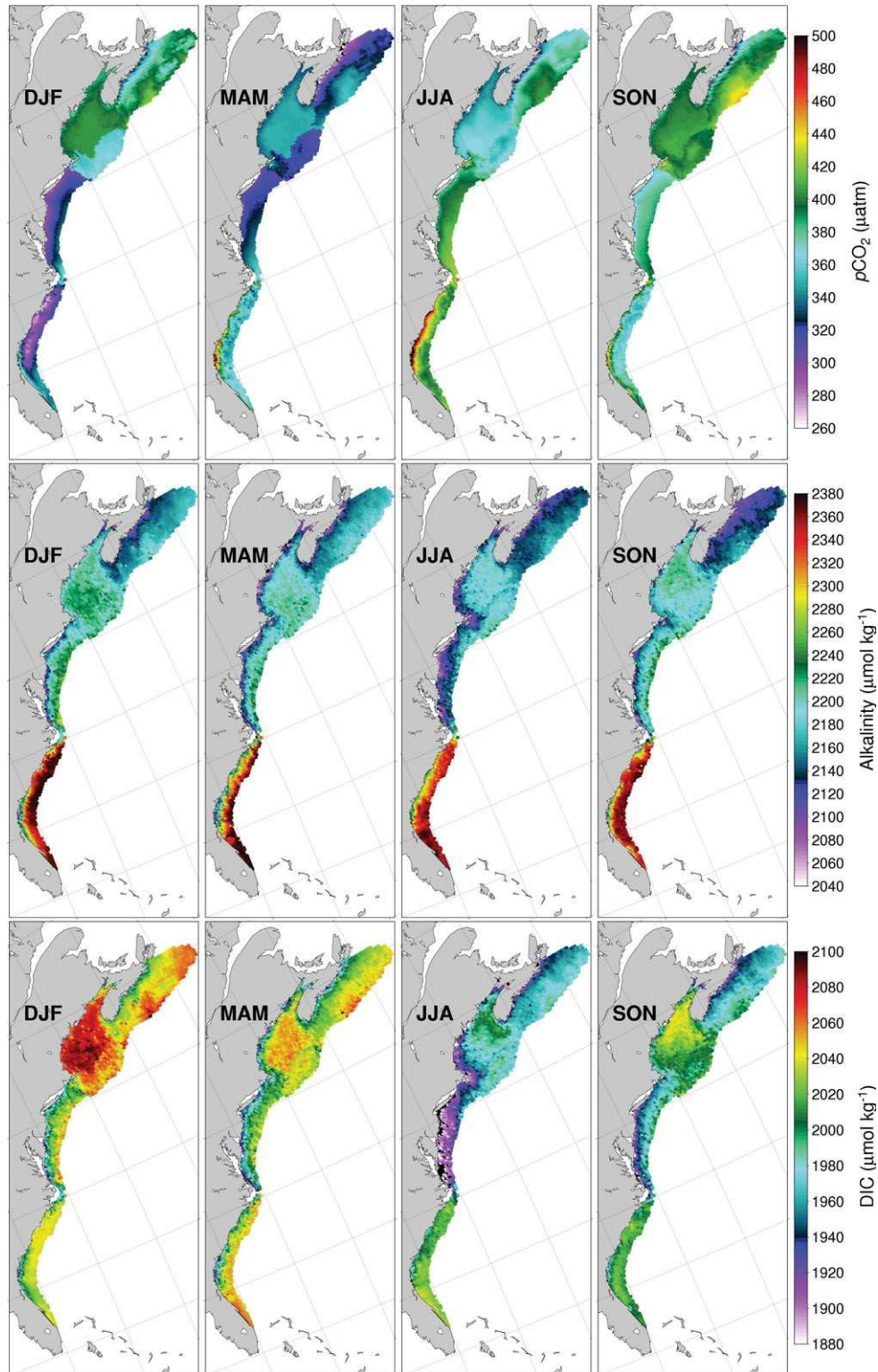


Figure 10. Seasonal maps of algorithm $p\text{CO}_2$, salinity-derived alkalinity from *Cai et al.* [2010] equations, and DIC derived from alkalinity and algorithm $p\text{CO}_2$. The seasons are defined as Dec-Jan-Feb (DJF), Mar-Apr-May (MAM), Jun-Jul-Aug (JJA), and Sep-Oct-Nov (SON).

biological drawdown in spring-summer. In contrast, the major contributing factor to the seasonal $p\text{CO}_2$ variability in the SAB is SST. Alkalinity influence is the third most important and salinity relatively the least influential. How-

ever, salinity has an impact in the statistical improvement of the $p\text{CO}_2$ algorithm, most pronounced in the SAB, which is a region where seasonal SSS variability is large (see Figure 2), especially on the inner shelf.

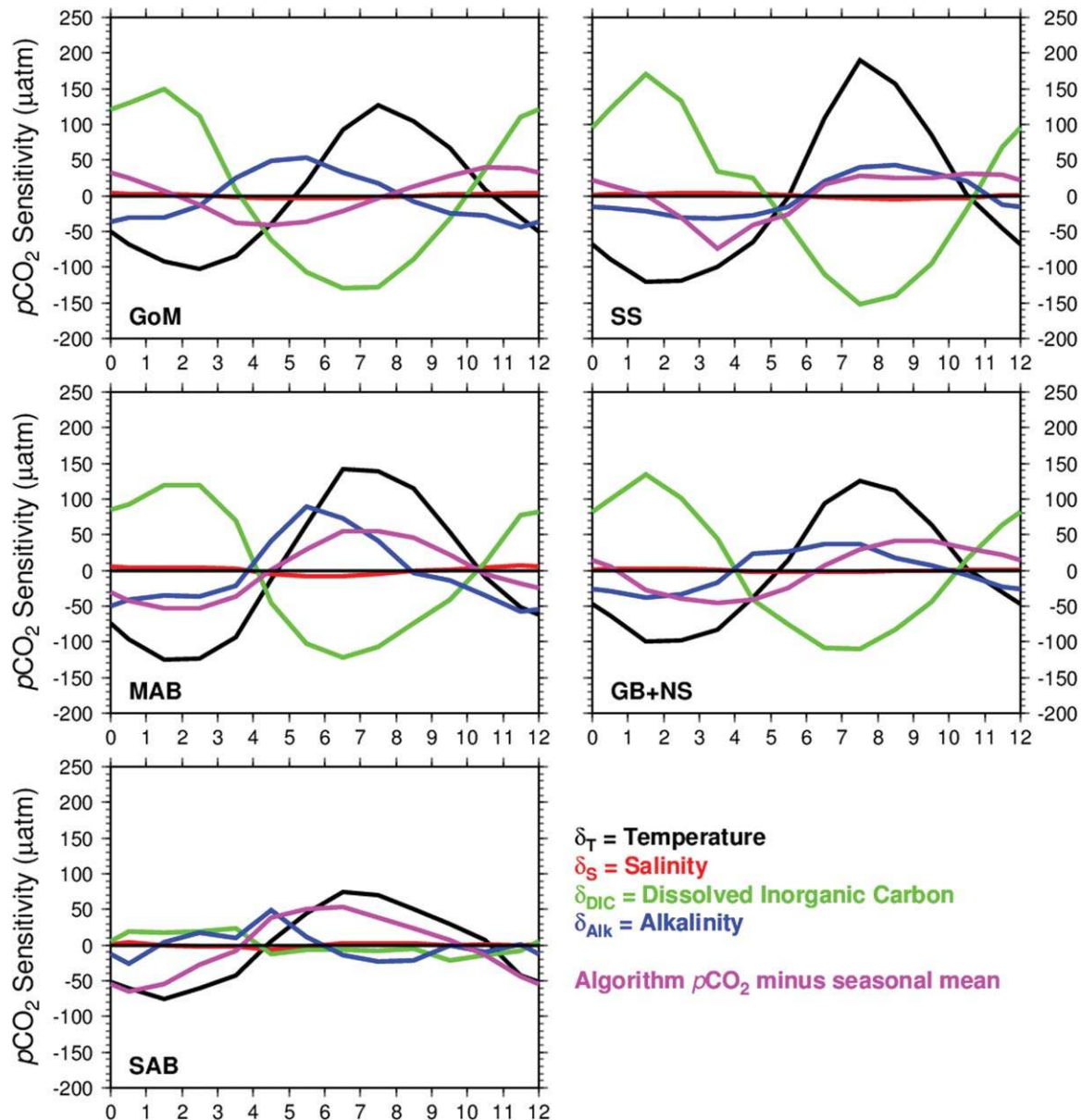


Figure 11. Sensitivity of $p\text{CO}_2$ seasonal cycle to most influential parameters. Alkalinity was derived using SSS from monthly WOA 2009 salinity data (D. Tomaso, personal communication, 2012), spatially interpolated using Kriging, and Cai *et al.* [2010] equations. DIC was derived from algorithm $p\text{CO}_2$, alkalinity, WOA SSS, and MODIS SST. Refer to text for methodology to derive parameter sensitivity.

[46] The seasonal DIC variability averaged for all five study regions, with the MLD superimposed, is shown in Figure 12. The four study regions north of Cape Hatteras (MAB, GoM, GB+NS, and SS) have distinct DIC seasonal cycles with amplitudes of 100–120 $\mu\text{mol kg}^{-1}$. Regionally averaged winter MLDs range from 30 m in the MAB to more than 100 m in the GoM. Deeper MLDs in winter/autumn, resulting from wind and convective mixing, is the major factor contributing to the elevated DIC concentrations (2010–2080 $\mu\text{mol kg}^{-1}$) shown during these seasons. The shoaling of the MLDs in spring-summer, together with the drawdown of CO₂ by biology, are the major factors driving the significant reduction in surface DIC. For instance, in the MAB the DIC drops from 2020 $\mu\text{mol kg}^{-1}$ in February–March to 1900 $\mu\text{mol kg}^{-1}$ in June. In addition

to biology and deep mixing, DIC, and consequently the surface ocean $p\text{CO}_2$, is also affected by sea-air exchange. In the GoM, for instance, there is a significant effect of the sea-air exchange on DIC when the $\Delta p\text{CO}_2$ is high and the mixed layer becomes very shallow (J. Salisbury, personal communication, 2012). The amplitudes of the seasonal MLD and DIC in the SAB are significantly less than in the other regions, most probably due to the shallower depths and much lower phytoplankton productivity.

4.4. Interannual Variability of Surface Ocean $p\text{CO}_2$ and Sea-Air Flux

[47] The interannual variability of surface ocean $p\text{CO}_2$ and sea-air CO₂ flux were calculated using the algorithm (equation (1)) with inputs from monthly satellite products

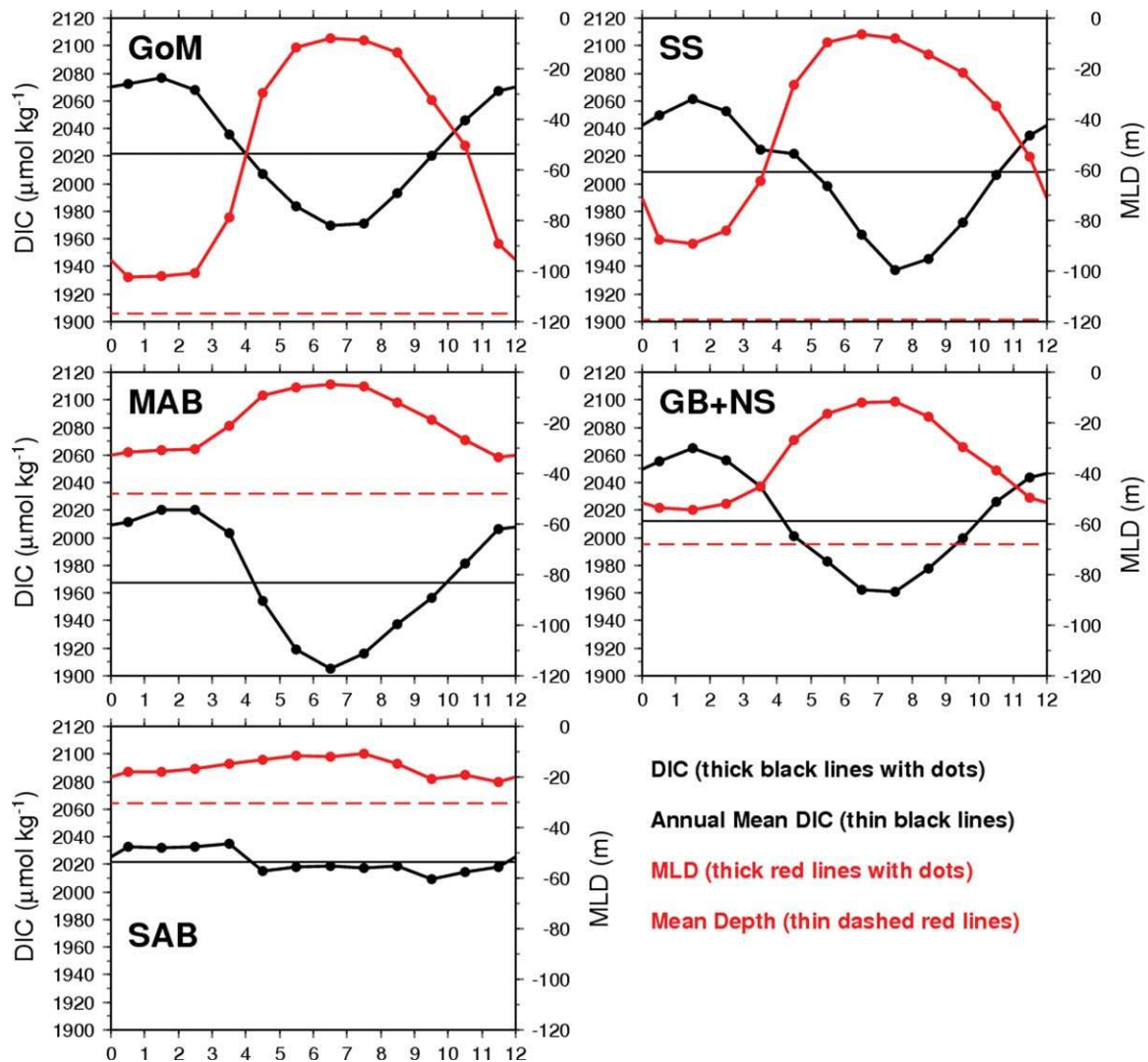


Figure 12. Regionally averaged seasonal DIC (black lines and circles) derived from TA (SSS) [Cai *et al.*, 2010], SST from MODIS, monthly SSS from WOA 2009 (D. Tomaso, personal communication, 2012) spatially interpolated using Kriging, and algorithm $p\text{CO}_2$. The seasonal mixed layer depth (MLD) is superposed for each region (red lines and circles). The red dashed lines represent the mean bottom depth for each region and the thin black lines are the annual mean DIC for each region, with the GoM and SAB having the highest values ($2022 \mu\text{mol kg}^{-1}$) and the MAB the lowest ($1968 \mu\text{mol kg}^{-1}$).

(SST and *Chl*) for 2003–2010 and climatologic SSS. The sea air flux was computed using monthly CCMP winds for the same period. The results are shown in Figure 13 ($p\text{CO}_2$ (left), sea-air flux (right)) and summarized in Table 3. Note that the algorithm results in Table 2 were derived using monthly satellite climatology of SST and *Chl*, and climatologic winds, while those in Table 3 are from monthly inter-annual satellite products and winds. The GoM and SS have the largest interannual variability in sea-air CO₂ flux. The flux in the SS is positive (source) in 2005 ($+0.15 \text{ Tg C yr}^{-1}$) and negative (weak sink) in 2006 ($-0.02 \text{ Tg C yr}^{-1}$), while the largest flux ($-1.55 \text{ Tg C yr}^{-1}$) occurred in 2007. These large differences in the SS annual fluxes are a result of large interannual changes in the spring drawdown of surface ocean $p\text{CO}_2$ (see Figure 13). However, in the GoM the

large differences in annual flux ($+0.17 \text{ Tg C yr}^{-1}$ in 2004 and $-0.19 \text{ Tg C yr}^{-1}$ in 2007) are a result of wind speed variability as there are not significant interannual changes in the surface ocean $p\text{CO}_2$ seasonal cycle, as shown in Figure 13.

[48] Averaged over the entire 8 years, the MAB, GB+NS, and SAB are relatively the largest sinks of CO₂ to the atmosphere (-2.1 , -1.0 , and $-0.9 \text{ Tg C yr}^{-1}$, respectively), while the GOM is a small source ($+0.01 \text{ Tg C yr}^{-1}$), albeit with large changes from year to year. The east coast uptake (mean over the 8 years) is $-4.6 \text{ Tg C yr}^{-1}$, which is at the upper end of the estimates from the binned field measurements with two different gas transfer parameterizations (-4.0 and $-4.3 \text{ Tg C yr}^{-1}$), and -3.6 and $-4.0 \text{ Tg C yr}^{-1}$).

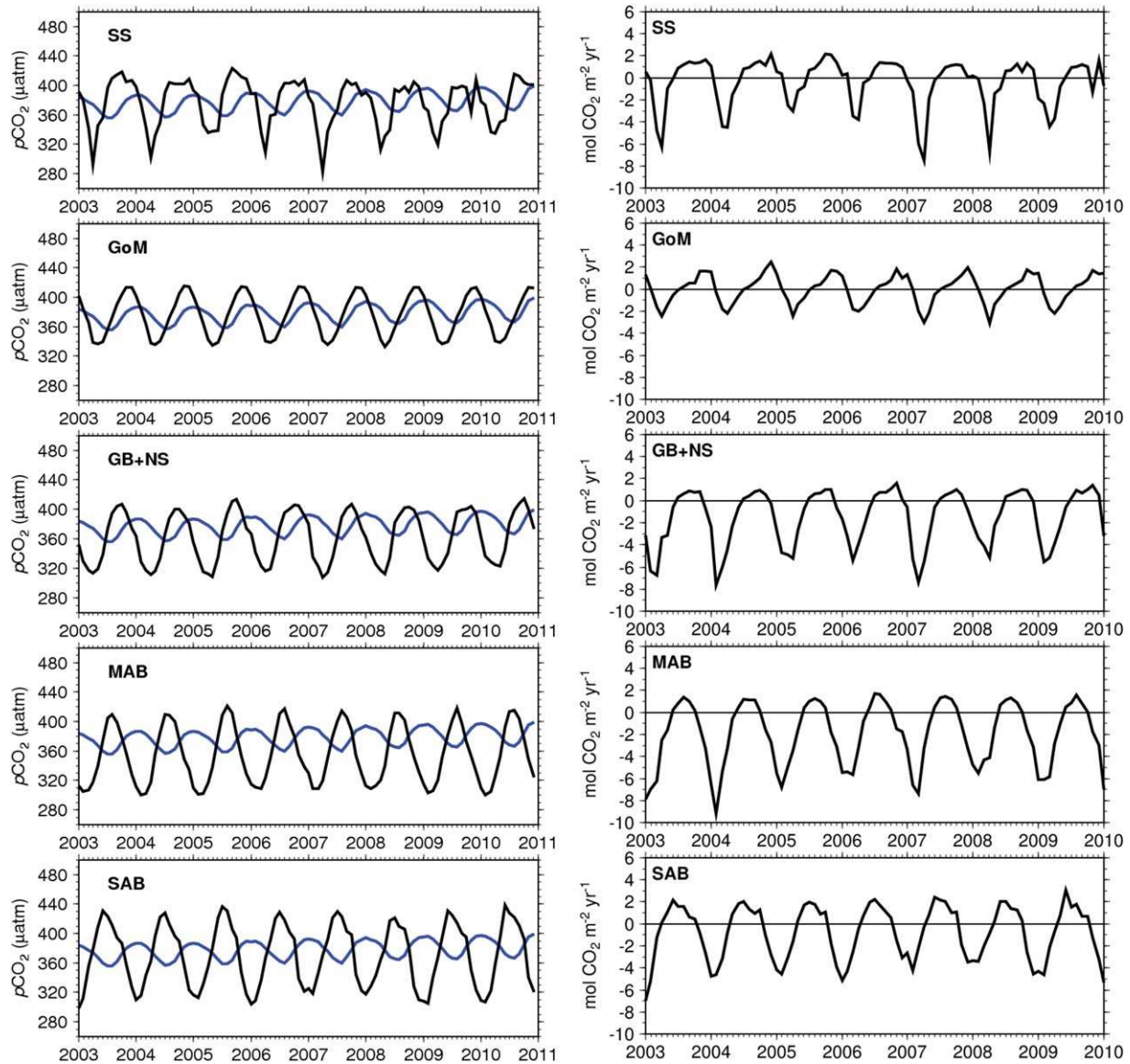


Figure 13. (left) Monthly surface ocean $p\text{CO}_2$ derived from algorithm (black lines) and atmospheric $p\text{CO}_2$ from Grifton, NC located at 35.53°N and 77.38°W (superposed blue lines). (right) Sea-air CO_2 flux derived from $\Delta p\text{CO}_2$, CCMP winds, and *Ho et al.* [2011] gas transfer parameterization.

yr^{-1} from the algorithm using monthly climatology inputs (see Table 2). Table 3 shows that the lowest estimate occur in 2006 ($-3.4 \text{ Tg C yr}^{-1}$) and the highest in 2007 ($-5.4 \text{ Tg C yr}^{-1}$).

[49] The interannual variability in sea-air flux in all regions is mostly due to changes in the surface ocean $p\text{CO}_2$, mainly in response to changes in solubility and biological drawdown due to variability in SST and phytoplankton production, respectively, and the wind-dependent gas exchange at the sea-air interface, accounted for by the gas transfer coefficient k_{660} (in cm h^{-1}). From Table 1, we see that the algorithm $p\text{CO}_2$ sensitivity to the input parameters varies significantly from region to region. In fact, the coefficients of many parameters change sign on a regional basis. So, in order to evaluate which parameters influenced

the resulting estimates of sea-air flux the most, one needs to examine the yearly changes of these parameters and evaluate how much influence they have on the $p\text{CO}_2$. As an example, there was a significant shift in the mean annual sea-air flux in the SS from 2005 to 2007 (Table 3 and Figure 14). In 2005 the SS was a weak source of atmospheric CO_2 ($+0.15 \text{ Tg C yr}^{-1}$), while in 2007 it shifted to a relatively strong CO_2 sink ($-1.55 \text{ Tg C yr}^{-1}$). This shift was associated with lower SST (-0.8°C), higher $\log_{10}[\text{Chl}]$ ($+0.067$), and higher k_{660} ($+2.19 \text{ cm hr}^{-1}$) on average in 2007 compared to 2005. Using the coefficients for SS in Table 1, $8.77 \pm 0.26 \mu\text{atm } (^\circ\text{C})^{-1}$, $-100.32 \pm 4.66 \mu\text{atm } (\log_{10}[\text{Chl}])^{-1}$, we get the following changes in $p\text{CO}_2$ in 2007 compared to 2005: $-7.1 \pm 0.2 \mu\text{atm}$ from SST and $-6.7 \pm 0.3 \mu\text{atm}$ from *Chl*, for a total decrease in surface

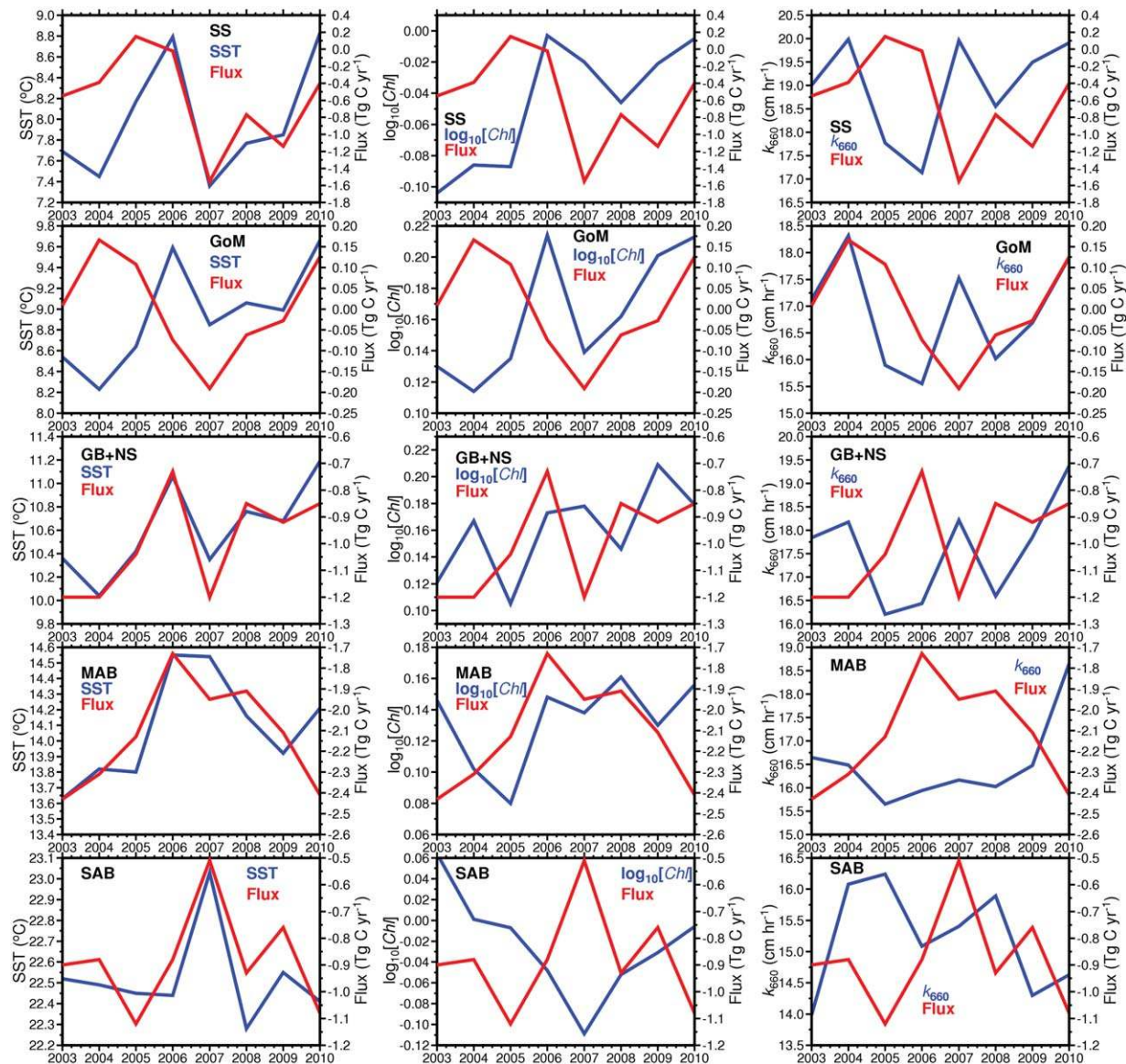


Figure 14. Mean annual sea-air CO₂ flux (red lines, Tg C yr⁻¹) combined with SST (°C), log₁₀[Chl] (blue lines) and k_{660} (cm h⁻¹, blue lines) for all five regions.

ocean $p\text{CO}_2$ of -13.8 ± 0.4 atm. Considering that this is a regionally and annually averaged value, this is a significant change in $p\text{CO}_2$, which, combined with the increase in k_{660} , is the main reason leading to changes in sea-air flux.

[50] Time series (2003–2010) of annual mean sea-air CO₂ flux averaged for each of the five regions, each combined with annual means of SST, log₁₀[Chl], and k_{660} , are shown in Figure 14. We show log₁₀[Chl] instead of absolute Chl concentration because the log-transformed Chl is the parameter used by the algorithm. Examination of each of these time series reveals some interesting interannual changes. The scale of variability for each variable changes from region to region, and it is reflected by adopting different vertical axis ranges for each region. Interestingly, 2006 is a year of transition for all regions north of Cape Hatteras (MAB, GB+NS, GoM, and SS). In 2006, the highest SST and Chl occur in the GoM and SS, followed by a decrease in SST reaching a minimum in 2007, which, combined

with a peak in k_{660} resulted in the largest uptake of CO₂ by the ocean in these two regions. As a result, there was a transition in the sea-air flux in the SS from a very weak sink in 2006 (-0.02 Tg C yr⁻¹) to a stronger sink in 2007 (-1.55 Tg C yr⁻¹). There was an increase of SST from 2007 to 2010 that contributed to a reduction in the ocean uptake. The sea-air flux interannual variability in the GB+NS, MAB, and SAB was also largely driven by changes in SST, with warmer years having reduced ocean uptake and colder years showing an increase in uptake.

[51] The annual mean time series of sea-air flux for each region (2003–2010), and the total for the entire east coast, are shown in Figure 15. The GoM and SS regions were relatively stronger sinks of CO₂ to the atmosphere in 2007 (-0.19 and -1.55 Tg C yr⁻¹, respectively). The annual uptake of CO₂ ranged from -0.51 to -1.12 Tg C yr⁻¹ in the SAB with a mean of -0.89 ± 0.18 Tg C yr⁻¹ for 2003–2010. The equivalent values for the GB+NS were similar,

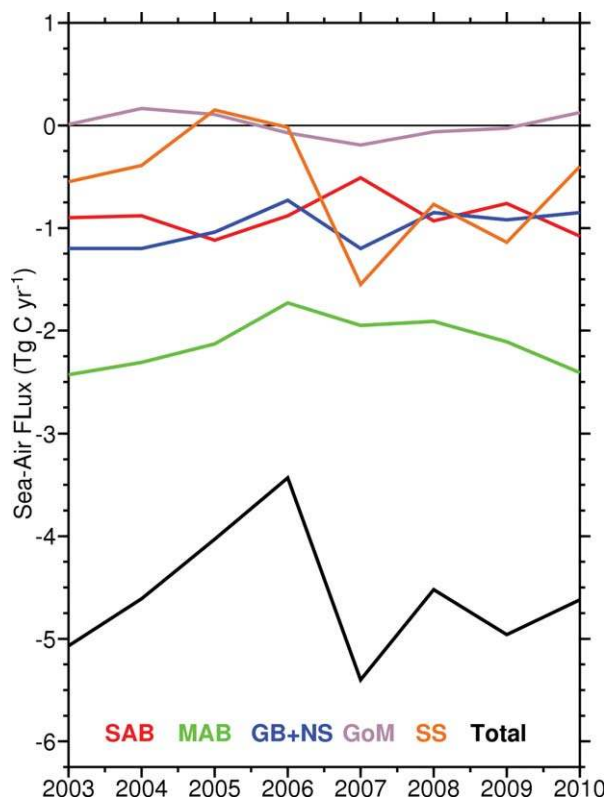


Figure 15. Time series of algorithm annual sea-air CO₂ flux for all five individual regions and for the entire east coast.

with a range of -0.73 to -1.20 Tg C yr⁻¹ and an overall mean of -1.00 ± 0.18 Tg C yr⁻¹. The MAB was the largest sink with values ranging from -1.73 to -2.43 Tg C yr⁻¹, and an overall mean of -2.12 ± 0.24 Tg C yr⁻¹. The total sea-air flux (sum of all five regions) ranged from -3.4 to -5.4 Tg C yr⁻¹, with the lowest uptake in 2006 and the highest in 2007.

5. Summary and Future Work

[52] We reconstructed a monthly climatology of surface ocean $p\text{CO}_2$ for the North American east coast continental shelf and developed regional algorithms to analyze the seasonal and interannual variability of surface ocean $p\text{CO}_2$ and sea-air CO₂ flux. A sensitivity analysis of parameters that influence the surface ocean $p\text{CO}_2$ showed that changes in DIC and SST are the main drivers for the $p\text{CO}_2$ seasonal cycle. Vertical mixing, mixing of low-salinity waters with shelf water, and biological drawdown are highly influential in the DIC variability. Much larger seasonal cycle amplitudes of DIC occur in regions north of Cape Hatteras than south of it. The annual sea-air CO₂ flux for the entire East Coast derived from the algorithm ranges from -3.4 Tg C yr⁻¹ (2006) to -5.4 Tg C yr⁻¹ (2007) during the analyzed period (2003–2010). In general, estimates from the binned data and algorithm are in agreement with previous studies when the range of uncertainty and interannual variability are taken into account.

[53] Uncertainties in the estimates of sea-air flux can be reduced by filling the spatial and temporal gaps in the exist-

ing surface ocean $p\text{CO}_2$ inventory for the U.S. east coast. The limitations of spatial and temporal surface ocean $p\text{CO}_2$ data coverage present a challenge in validating algorithms and biogeochemical model $p\text{CO}_2$ and sea-air flux estimates. Improvements can only be obtained by continuous monitoring of $p\text{CO}_2$ and other carbon cycle related variables in the nearshore and shelf regions of the U.S. east coast. As shown in Figure 3, all regions have major spatial and temporal gaps in the data coverage.

[54] In this study, we used a multiple regression approach to convert regional satellite observed quantities (SST and *Chl*) into $p\text{CO}_2$. However, the relationship $p\text{CO}_2 = f(\text{SST}, \text{Chl}, \text{SSS}, \text{time})$ is empirical and does not represent a unique solution as $p\text{CO}_2$ depends on factors other than local SST and *Chl*, for instance. Surface waters with identical SST and *Chl* can possibly have different $p\text{CO}_2$ levels. However, there have been studies that apply the technique of neural networks for mapping in situ $p\text{CO}_2$ data in the open ocean [Friedrich and Oschlies, 2009; Lefèvre et al., 2005; Telszewski et al., 2009]. The advantage of the neural network approach is that it can recognize and exploit relationships in the data which are not predefined (as in regression techniques) and need to be expressible by an equation. This makes neural networks particularly suited to mapping relationships that are nonlinear and empirical, provided sufficient data are available to “train” the network. This technique looks promising for mapping the surface ocean $p\text{CO}_2$ in other coastal regions as well.

[55] Hales et al. [2012] presented a method for predicting coastal surface-water $p\text{CO}_2$ from remote sensing data, based on self-organizing maps (SOMs) and a nonlinear semiempirical model of surface water carbonate chemistry, a method potentially applicable to the coastal regions in this study. The SOM approach was used to objectively map the subregions, while an entirely different approach was used to develop the $p\text{CO}_2$ algorithm within the SOM-defined subregions. The model used simple empirical relationships between carbonate chemistry (DIC and Alk) and satellite data (SST and *Chl*). Surface water $p\text{CO}_2$ was calculated from the empirically predicted DIC and Alk. This directly incorporated the inherent nonlinearities of the carbonate system, in a completely mechanistic manner.

Appendix A: Additional Sources of Surface Ocean $p\text{CO}_2$ Not Included in the SOCAT Data

A1. South Atlantic Bight

[56] Underway surface ocean $p\text{CO}_2$ data from the SAB were collected by Dr. Wei-Jun Cai (a coauthor in this study) and coworkers at the Department of Marine Sciences, University of Georgia. A total of 65,454 underway surface ocean $p\text{CO}_2$ records were processed for this study from six cruises along the SAB continental shelf: 5–16 January 2005, 19–30 March 2005, 27 July to 5 August 2005, 7–17 October 2005, 16–21 December 2005, and 17–27 May 2006. The SOCAT data set includes the 2005 cruises but not those undertaken in 2006, which were added to our analysis to include all cruises. In all of the sampling cruises except for the one in December 2005, the research vessel transected the whole SAB from coastline to about 500 m water depth. The survey focused on five cross-shelf

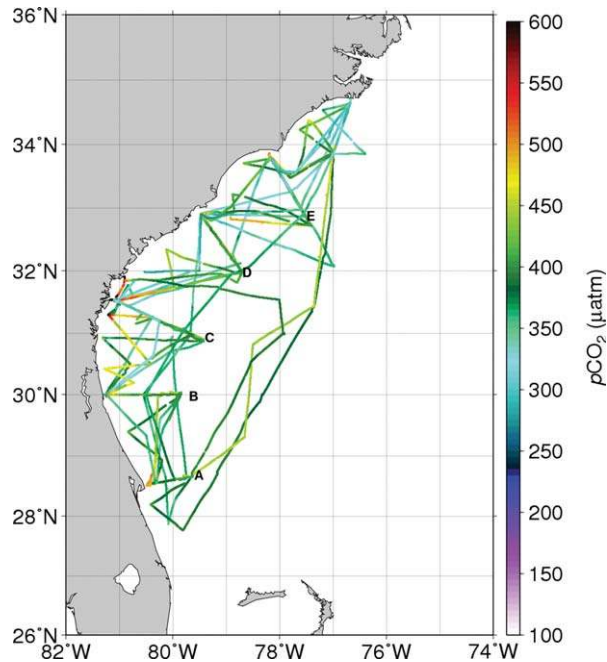


Figure A1. Distribution of underway $p\text{CO}_2$ tracks in the SAB.

transects that are named E-, D-, C-, B-, and A-transect, respectively, from north to south. In December 2005, the ship transected the whole SAB, but did not cover D- and B-transects and did not go beyond the 200 m isobaths due to limited ship time. Surface water and atmospheric $x\text{CO}_2$ were measured underway during all cruises. Sea surface temperature (SST) and salinity were recorded continuously with an onboard SeaBird flow through thermosalinograph. Sea level pressure was recorded using an onboard R.M. Young barometric pressure sensor. Surface water $x\text{CO}_2$ was measured using a LI-COR 7000 infrared gas analyzer coupled to a gas-water equilibrator. Details of the methodology and accuracy of instruments used are given in Jiang *et al.* [2008]. Figure A1 shows the data distribution map.

A2. Gulf of Maine

[57] Underway surface ocean $p\text{CO}_2$ data from monthly cruises in the southern Gulf of Maine were obtained from the University of New Hampshire (UNH) and integrated with the SOCAT data base. Underway data are measured continuously from pumped surface water for physical, chemical, biological and biooptical properties. The data used in this study consisted of 309,665 surface observations spanning the period of 2004–2010. These data originate from the UNH Coastal Ocean Observing Center's Coastal Carbon Group, which is an interdisciplinary research team within UNH-EOS engaged in efforts to observe and model how the Earth's pool of carbon moves between the land, ocean, and atmosphere with a particular focus on how this carbon cycling occurs in coastal regions, such as the Gulf of Maine. Dr. Joe Salisbury, a coauthor in this study, is a member of the UNH Coastal Carbon Group. The methodology and instrumentation details are given in Vandemark *et al.* [2011]. The precision of the $f\text{CO}_2$ measurements was ± 3 μatm . Figure A2 shows the data distribution map. All

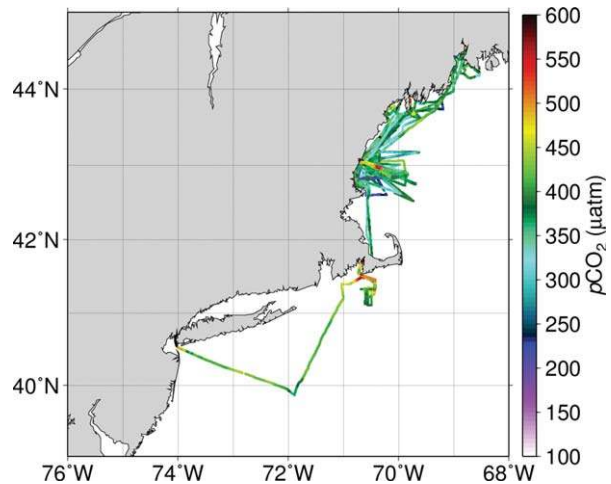


Figure A2. Map showing the underway $p\text{CO}_2$ tracks in the GoM and a single cruise track from Woods Hole to New York City.

underway cruise tracks are in the GoM, except for a single cruise track from Woods Hole to New York City.

A3. Scotian Shelf

[58] Underway (UW) surface ocean $p\text{CO}_2$ data from transects across the Scotian Shelf, and high-frequency $p\text{CO}_2$, SST, SSS, and calibrated fluorometer Chl data from the CARIOCA buoy were obtained from Dalhousie University [Shadwick *et al.*, 2010, 2011]. These data were used to evaluate the algorithm performance on the Scotian Shelf. Hourly, autonomous observations of surface water $p\text{CO}_2$ (μatm), chlorophyll-*a* fluorescence (F_{Chl}), and SST, were made using a CARIOCA buoy moored roughly 30 km offshore from Halifax, at 44.3°N and 63.3°W, between April 2007 and June 2008. Hourly CARIOCA data were uploaded and transmitted daily via the ARGOS satellite system. The $p\text{CO}_2$ measurements were made by an automated spectrophotometric technique. A Sea-Bird (SBE 41) conductivity and temperature sensor was used to measure temperature ($\sim\text{C}$) and to determine salinity; chlorophyll-*a* fluorescence ($\mu\text{g L}^{-1}$) was determined by a WET Labs miniature fluorometer (WETstar). Nonphotochemical effects that are related to the intensity of the incoming solar radiation may decrease F_{Chl} up to 80% during the day. This effect can be avoided by using night-time data which, to a large extent, are free of the effects of nonphotochemical quenching, for fluorometer calibration. Night-time data were taken as a mean F_{Chl} between 03:00 and 06:00 UTC (or 11:00 and 02:00 LT); data points were temporally interpolated to match discrete chlorophyll-*a* measurements (Chl-*a* in mg m^{-3}) from monthly or twice monthly occupations at the mooring site. Chl-*a* concentration was determined fluorometrically in a Turner Designs fluorometer using the acid ratio technique for seawater samples collected at 3, 5, or 10 m depth. A linear regression ($r^2 = 0.76$, $N = 29$, $p < 0.001$) was used to determine the relationship between the F_{Chl} and Chl-*a*, and applied to the CARIOCA fluorescence-derived Chl-*a* time-series (Chl_F in mg m^{-3}). Shadwick *et al.* [2010] performed a validation of satellite

monthly chlorophyll data by regressing it against the (night-time calibrated), monthly mean, CARIOCA Chl_F time series ($r^2 = 0.68$, $N = 14$, $p < 0.002$).

[59] Measurements of $p\text{CO}_2$ UW were made by a continuous flow equilibration system in: October 2006, April, August, and October 2007, and April and October, 2008 on board the *CCGS Hudson*. The UW measurements (see distribution map in Figure 7a) were obtained on monitoring cruises on the Scotian Shelf (see *Shadwick et al.* [2011] for details of the field program). Measurements of $p\text{CO}_2$ UW were made by a nondispersive, infrared spectrometer (LiCor, LI-7000). The system was located in the aft-laboratory of the ship and the intake depth was approximately 3 m below the water surface. Measurements were made every minute and used to compute hourly averages. The system was calibrated daily with both a CO₂-free reference gas (N₂) and a CO₂ calibration gas (328.99 ppm) provided by the U.S. National Oceanic and Atmospheric Administration (NOAA). The data were corrected to in situ water temperature and to 100% humidity and had an associated uncertainty of less than 1 μatm .

[60] **Acknowledgments.** We wish to acknowledge the NASA Ocean Biology and Biogeochemistry program for providing funds for this project. We also want to acknowledge Daniel Tomaso for providing the compiled climatologic data sets for sea surface salinity and mixed layer depth, and Environment Canada for making available the wind data from Sable Island.

References

- Alberts, J. J., and M. Takacs (1999), Importance of humic substances for carbon and nitrogen transport into southeastern United States estuaries, *Org. Geochem.*, *30*(6), 385–395.
- Atlas, R., R. N. Hoffman, J. Ardizzone, S. M. Leidner, J. C. Jusem, D. K. Smith, and D. Gombos (2011), A cross-calibrated, multiplatform ocean surface wind velocity product for meteorological and oceanographic applications, *Bull. Am. Meteorol. Soc.*, *92*, 157–174, doi:10.1175/2010BAMS2946.1.
- Borges, A. V. (2005), Do we have enough pieces of the jigsaw to integrate CO₂ fluxes in the coastal ocean?, *Estuaries*, *28*(1), 3–27.
- Borges, A. V., B. Delille, and M. Frankignoulle (2005), Budgeting sinks and sources of CO₂ in the coastal ocean: Diversity of ecosystems counts, *Geophys. Res. Lett.*, *32*, L14601, doi:10.1029/2005GL023053.
- Borges, A. V., B. Tilbrook, N. Metzl, A. Lenton, and B. Delille (2008), Inter-annual variability of the carbon dioxide oceanic sink south of Tasmania, *Biogeosciences*, *5*(1), 141–155.
- Cai, W. J. (2011), Estuarine and coastal ocean carbon paradox: CO₂ sinks or sites of terrestrial carbon incineration?, in *Annual Review of Marine Science*, vol. 3, edited by C. A. Carlson and S. J. Giovannoni, pp. 123–145, Annu. Rev., Palo Alto, Calif.
- Cai, W.-J., Y. Wang, and R. E. Hodson (1998), Acid-base properties of dissolved organic matter in the estuarine waters of Georgia, *Geochim. Cosmochim. Acta*, *62*, 473–483.
- Cai, W. J., M. H. Dai, and Y. C. Wang (2006), Air-sea exchange of carbon dioxide in ocean margins: A province-based synthesis, *Geophys. Res. Lett.*, *33*, L12603, doi:10.1029/2006GL026219.
- Cai, W. J., X. P. Hu, W. J. Huang, L. Q. Jiang, Y. C. Wang, T. H. Peng, and X. Zhang (2010), Alkalinity distribution in the western North Atlantic Ocean margins, *J. Geophys. Res.*, *115*, C08014, doi:10.1029/2009JC005482.
- Chapman, D. C., and R. C. Beardsley (1989), On the origin of shelf water in the middle Atlantic bight, *J. Phys. Oceanogr.*, *19*(3), 384–391.
- Craig, S. E., H. Thomas, C. T. Jones, W. K. W. Li, B. J. W. Greenan, E. H. Shadwick, and W. J. Burt (2013), Temperature and phytoplankton cell size regulate carbon uptake and carbon overconsumption in the ocean, *Biogeosci. Discuss.*, *10*, 11,255–11,282, doi:10.5194/bgd-10-11255-2013.
- DeGrandpre, M. D., G. J. Olbu, C. M. Beatty, and T. R. Hammar (2002), Air-sea CO₂ fluxes on the US Middle Atlantic Bight, *Deep Sea Res. Part II*, *49*(20), 4355–4367.
- Dickson, A. G. (1990), Standard potential of the reaction – AgCl(S)+1/2H₂(G)=Ag(S)+HCl(aq) and the standard acidity constant of the ion HSO₄[–] in synthetic sea-water from 273.15°K to 318.15°K, *J. Chem. Thermodyn.*, *22*(2), 113–127.
- Dickson, A. G., and F. J. Millero (1987), A comparison of the equilibrium constants for the dissociation of carbonic acid in seawater media, *Deep Sea Res. Part A*, *34*(10), 1733–1743.
- Fox, M. F., D. R. Kester, and J. A. Yoder (2005), Spatial and temporal distributions of surface temperature and chlorophyll in the Gulf of Maine during 1998 using SeaWiFS and AVHRR imager, *Mar. Chem.*, *97*(1–2), 104–123.
- Frankignoulle, M., and A. V. Borges (2001), European continental shelf as a significant sink for atmospheric carbon dioxide, *Global Biogeochem. Cycles*, *15*(3), 569–576.
- Friedrich, T., and A. Oschlies (2009), Neural network-based estimates of North Atlantic surface $p\text{CO}_2$ from satellite data: A methodological study, *J. Geophys. Res.*, *114*, C03020, doi:10.1029/2007JC004646.
- GLOBALVIEW-CO₂ (2011), Cooperative atmospheric data integration project—carbon dioxide, NOAA ESRL, Boulder, Colo. [Available at ftp.cmdl.noaa.gov, Path: ccg/co2/GLOBALVIEW.]
- Hales, B., C. Wei-Jun, B. Greg Mitchell, C. L. Sabine, and O. Schofield (Eds.) (2008), North American Continental Margins: A Synthesis and Planning Workshop, Report of the North American Continental Margins Working Group for the U.S. Carbon Cycle Scientific Steering Group and Interagency Working Group, 110 pp., U.S. Carbon Cycle Sci. Prog., Washington, D. C.
- Hales, B., P. G. Strutton, M. Saraceno, R. Letelier, T. Takahashi, R. A. Feely, C. L. Sabine, and F. Chavez (2012), Satellite-based prediction of $p\text{CO}_2$ in coastal waters of the eastern North Pacific, *Progr. Oceanogr.*, *103*, 1–15, doi:10.1016/j.pocean.2012.03.001.
- Ho, D. T., R. Wanninkhof, P. Schlosser, D. S. Ullman, D. Hebert, and K. F. Sullivan (2011), Toward a universal relationship between wind speed and gas exchange: Gas transfer velocities measured with ³He/SF₆ during the Southern Ocean gas exchange experiment, *J. Geophys. Res.*, *116*, C00F04, doi:10.1029/2010JC006854.
- Hofmann, E., et al. (2008), Eastern US continental shelf carbon budget integrating models, data assimilation, and analysis, *Oceanography*, *21*(1), 86–104.
- Hofmann, E. E., et al. (2011), Modeling the dynamics of continental shelf carbon, in *Annual Review of Marine Science*, vol. 3, edited by C. A. Carlson and S. J. Giovannoni, pp. 93–122, Annu. Rev., Palo Alto, Calif.
- Jiang, L.-Q., W.-J. Cai, R. Wanninkhof, Y. Wang, and H. Lüger (2008), Air-sea CO₂ fluxes on the U.S. South Atlantic Bight: Spatial and seasonal variability, *J. Geophys. Res.*, *113*, C07019, doi:10.1029/2007JC004366.
- Jiang, L.-Q., W.-J. Cai, Y. Wang, and J. E. Bauer (2013), Influence of terrestrial inputs on continental shelf carbon dioxide, *Biogeosciences*, *10*, 839–849, doi:10.5194/bg-10-839-2013.
- Joyce, T. M., J. K. B. Bishop, and O. B. Brown (1992), Observations of offshore shelf-water transport induced by a warm-core ring, *Deep Sea Res. Part I*, *39*(1A), S97–S113.
- Kalnay, E., et al. (1996), The NCEP/NCAR 40-year reanalysis project, *Bull. Am. Meteorol. Soc.*, *77*(3), 437–471.
- Laruelle, G. G., H. H. Durr, C. P. Slomp, and A. V. Borges (2010), Evaluation of sinks and sources of CO₂ in the global coastal ocean using a spatially-explicit typology of estuaries and continental shelves, *Geophys. Res. Lett.*, *37*, L15607, doi:10.1029/2010GL043691.
- Lefèvre, N., A. J. Watson, and A. R. Watson (2005), A comparison of multiple regression and neural network techniques for mapping in situ $p\text{CO}_2$ data, *Tellus Ser. B*, *57*(5), 375–384.
- Le Queré, C., T. Takahashi, E. T. Buitenhuis, C. Rodenbeck, and S. C. Sutherland (2010), Impact of climate change and variability on the global oceanic sink of CO₂, *Global Biogeochem. Cycles*, *24*, GB4007, doi:10.1029/2009GB003599.
- Lohrenz, S. E., and W. J. Cai (2006), Satellite ocean color assessment of air-sea fluxes of CO₂ in a river-dominated coastal margin, *Geophys. Res. Lett.*, *33*, L01601, doi:10.1029/2005GL023942.
- O'Reilly, J. E., and C. Zetlin (1998), Seasonal, horizontal, and vertical distribution of phytoplankton chlorophyll a in the northeast U.S. continental shelf ecosystem, in *Fishery Bulletin*, p. 120, NOAA, Silver Spring, Md.

- Pfeil, B., et al. (2012), A uniform, quality controlled surface ocean CO₂ Atlas (SOCAT), *Earth Syst. Sci. Data Discuss.*, 5, 735–780, doi:10.5194/essdd-5-735-2012.
- Rosby, T. (1987), On the energetics of the gulf stream at 73W, *J. Mar. Res.*, 45(1), 59–82.
- Salisbury, J. E., D. Vandemark, C. W. Hunt, J. W. Campbell, W. R. McGillis, and W. H. McDowell (2008), Seasonal observations of surface waters in two Gulf of Maine estuary-plume systems: Relationships between watershed attributes, optical measurements and surface pCO₂, *Estuarine Coastal Shelf Sci.*, 77(2), 245–252.
- Shadwick, E. H., H. Thomas, A. Comeau, S. E. Craig, C. W. Hunt, and J. E. Salisbury (2010), Air-sea CO₂ fluxes on the Scotian Shelf: Seasonal to multi-annual variability, *Biogeosciences*, 7(11), 3851–3867.
- Shadwick, E. H., H. Thomas, K. Azetsu-Scott, B. J. W. Greenan, E. Head, and E. Horne (2011), Seasonal variability of dissolved inorganic carbon and surface water pCO₂ in the Scotian Shelf region of the Northwestern Atlantic, *Mar. Chem.*, 124(1-4), 23–37.
- Shearman, R. K., and S. J. Lentz (2004), Observations of tidal variability on the New England shelf, *J. Geophys. Res.*, 109, C06010, doi:10.1029/2003JC001972.
- Signorini, S. R., and C. R. McClain (2007), Large-scale forcing impact on biomass variability in the South Atlantic Bight, *Geophys. Res. Lett.*, 34, L21605, doi:10.1029/2007GL031121.
- Smith, W. H. F., and P. Wessel (1990), Gridding with continuous curvature splines in tension, *Geophysics*, 55, 293–305.
- Takahashi, T., et al. (2009), Climatological mean and decadal change in surface ocean pCO₂, and net sea-air CO₂ flux over the global oceans, *Deep Sea Res. Part II*, 56, 554–577.
- Telszewski, M., et al. (2009), Estimating the monthly pCO₂ distribution in the North Atlantic using a self-organizing neural network, *Biogeosciences*, 6(8), 1405–1421.
- Thomas, H., Y. Bozec, K. Elkalay, and H. J. W. de Baar (2004), Enhanced open ocean storage of CO₂ from shelf sea pumping, *Science*, 304(1005), 1005–1008, doi:10.1126/science.1095491.
- Thomas, H., and A. V. Borges (2012), Biogeochemistry of coastal seas and continental shelves—Including biogeochemistry during the International Polar Year, *Estuarine Coastal Shelf Sci.*, 100, 1–2.
- Thomas, A. C., D. W. Townsend, and R. Weatherbee (2003), Satellite-measured phytoplankton variability in the Gulf of Maine, *Cont. Shelf Res.*, 23(10), 971–989.
- Thomas, H., L. S. Schiettecatte, K. Suykens, Y. J. M. Kone, E. H. Shadwick, A. E. F. Prowe, Y. Bozec, H. J. W. de Baar, and A. V. Borges (2009), Enhanced ocean carbon storage from anaerobic alkalinity generation in coastal sediments, *Biogeosciences*, 6(2), 267–274.
- Thomas, H., S. E. Craig, B. J. W. Greenan, W. Burt, G. J. Herndl, S. Higinson, L. Salt, E. H. Shadwick, and J. Urrego-Blanco (2012), Direct observations of diel biological CO₂ fixation on the Scotian Shelf, northwestern Atlantic Ocean, *Biogeosciences*, 9, 2301–2309, doi:10.5194/bg-9-2301-2012.
- Upstrom, L. (1974), Boron/chlorinity ratio of deep-sea water from Pacific Ocean, *Deep Sea Res.*, 21(2), 161–162, doi:10.1016/0011-7471(74)90074-6.
- Vandemark, D., J. E. Salisbury, C. W. Hunt, S. M. Shellito, J. D. Irish, W. R. McGillis, C. L. Sabine, and S. M. Maenner (2011), Temporal and spatial dynamics of CO₂ air-sea flux in the Gulf of Maine, *J. Geophys. Res.*, 116, C01012, doi:10.1029/2010JC006408.
- Verity, P. G., J. E. Bauer, C. N. Flagg, D. J. DeMaster, and D. J. Repeta (2002), The Ocean Margins Program: An interdisciplinary study of carbon sources, transformations, and sinks in a temperate continental margin system, *Deep Sea Res. Part II*, 49(20), 4273–4295.
- Wang, Z. A., W. J. Cai, Y. C. Wang, and H. W. Ji (2005), The southeastern continental shelf of the United States as an atmospheric CO₂ source and an exporter of inorganic carbon to the ocean, *Cont. Shelf Res.*, 25(16), 1917–1941.
- Wang, Z. A., R. Wanninkhof, W. J. Cai, R. H. Byrne, X. Hu, T. H. Peng, and W. J. Huang (2013), The marine inorganic carbon system along the Gulf of Mexico and Atlantic Coasts of the United States: Insights from a transregional coastal carbon study, *Limnol. Oceanogr.*, 58, 325–342.
- Wang, Z. H. A., and W. J. Cai (2004), Carbon dioxide degassing and inorganic carbon export from a marsh-dominated estuary (the Duplin River): A marsh CO₂ pump, *Limnol. Oceanogr.*, 49(2), 341–354.
- Wanninkhof, R., W. E. Asher, D. T. Ho, C. Sweeney, and W. McGillis (2009), Advances in quantifying air-sea gas exchange and environmental forcing, *Annu. Rev. Mar. Sci.*, 1, 213–244.
- Wessel, P., and W. H. F. Smith (1991), Free software helps map and display data, *Eos Trans. AGU*, 72, 441–446, doi:10.1029/90EO00319.
- Whitney, M. M. (2010), A study on river discharge and salinity variability in the Middle Atlantic Bight and Long Island Sound, *Cont. Shelf Res.*, 30(3-4), 305–318.